

# Daily Drought Prediction in the Huaihe River Basin Using VMD-informer-LSTM

Min Li<sup>1,2</sup>, Ming Ou<sup>1</sup>, Yuhang Yao<sup>1</sup>, Changman Yin<sup>1</sup>

<sup>1</sup> College of Hydraulic Science and Engineering, Yangzhou University, Yangzhou, China, 225000

<sup>2</sup> National Key Laboratory of Water Disaster Prevention, Hohai University, Nanjing, China,  
210098

Correspondence to: Min Li (limintju@126.com)

## Abstract

Accurate drought prediction is a key challenge in water resource management and agricultural planning. This study proposes a novel drought prediction framework that integrates Variational Mode Decomposition (VMD), Informer, and Long Short-Term Memory (LSTM) networks to enhance hydrological drought forecasting in the Huaihe River Basin, China. The VMD-Informer-LSTM model decomposes complex non-stationary drought sequences into multi-scale components, effectively extracting long-term trends and short-term fluctuations. Results show that the model outperforms LSTM, Transformer-LSTM, and Informer-LSTM, improving  $R^2$ , RMSE, MAE, and MAPE by 28.4%, 46.2%, 46.5%, and 50.8%, respectively, over the baseline LSTM. When the prediction period is 30 days, the VMD-Informer-LSTM achieves the highest prediction accuracy. During the 120–180 day prediction period, the prediction accuracy of all models declines, with drought intensity generally underestimated. Misclassifications are mainly concentrated in the transition zones between humid and semi-humid regions, with higher error frequency in semi-humid areas. Prediction accuracy is highest in the upstream and downstream regions, followed by the Yishuisi River Basin, while the midstream region performs poorly due to human interference. Shapley Additive Explanations (SHAP) further reveal that precipitation and temperature are the dominant meteorological drivers, jointly accounting for nearly half of the model's predictive power. These results confirm that the VMD-Informer-LSTM provides the most accurate predictions among the tested models, offering valuable support for drought risk assessment and water resource management in the Huaihe River Basin and other similar regions.

**Keywords:** Drought prediction, DEDI, Variational Mode Decomposition, informer, LSTM

## 1 Introduction

Drought represents one of the most spatially extensive, temporally persistent, and far-reaching natural disasters globally, with complex formation mechanisms involving intricate interactions between atmospheric circulation patterns, land surface processes, and human activities (Alsubih et al., 2021; Dai, 2013). Drought events not only directly threaten watershed water security and agricultural productivity but also profoundly affect regional ecosystem stability and socioeconomic development (Zhang et al., 2018). With intensifying climate change and increasing human activity intensity, drought events exhibit significant upward trends in frequency, intensity, and spatial extent (Cook et al., 2020; Trenberth et al., 2014). Therefore, accurate drought prediction is crucial for developing scientific disaster mitigation strategies, optimizing water resource allocation schemes,

39 and ensuring regional food and ecological security.

40 However, drought prediction faces major challenges due to the inherent complexity of drought  
41 phenomena (Hao et al., 2017). Drought occurrence and evolution are controlled by multiple natural  
42 and anthropogenic factors, including precipitation distribution, evapotranspiration processes,  
43 topographic conditions, land use changes, and human interventions (AghaKouchak et al., 2015;  
44 Vicente-Serrano et al., 2018). These factors generate highly complex, nonlinear, and non-stationary  
45 spatiotemporal evolution patterns. Drought time series typically contain multi-scale periodic  
46 oscillations, long-term trend changes, and stochastic fluctuation components that are mutually  
47 coupled and interdependent, forming extremely complex dynamical systems (Belayneh et al., 2014;  
48 Huang et al., 2015).

49 Traditional drought prediction methods rely on physics-based numerical models and st  
50 atistical regression approaches (Dutra et al., 2014; Yuan & Quiring, 2017). Physics-based  
51 methods include Global Climate Models (GCMs) such as the ECMWF and NCEP-CFSv2,  
52 which can provide global-scale long-term climate predictions but have coarse spatial resolu  
53 tions (typically 100-200 km) and cannot adequately capture regional drought characteristics  
54 (Saha et al., 2014). Regional Climate Models (RCMs) employ dynamic downscaling techni  
55 ques to achieve high resolutions (10-50 km) but inherit systematic biases from driving mo  
56 dels and require substantial computational resources (Jacob et al., 2014; Rummukainen, 20  
57 10). Land surface models such as Variable Infiltration Capacity (VIC), Community Land  
58 Model (CLM), and Noah simulate coupled water cycle, energy balance, and vegetation dyn  
59 amics processes but are highly sensitive to meteorological forcing data quality and paramet  
60 erization schemes (Ek et al., 2003; Lawrence et al., 2011). Statistical methods include line  
61 ar regression approaches, time series analysis and spectral/wavelet analysis techniques, etc  
62 (Box et al., 2015; Modarres, 2007). Time series models, such as Autoregressive Moving A  
63 verage (ARMA), Autoregressive Integrated Moving Average (ARIMA) models, Random Fo  
64 rest (RF), demonstrate certain capabilities for stationary time series. However, their predicti  
65 on performance significantly deteriorates on non-stationary, multi-periodic drought sequen  
66 ces (Mishra & Desai, 2005; Mossad & Alazba, 2015). Despite contributions from these tradi  
67 tional methods, fundamental limitations persist across both physics-based and statistical app  
68 roaches (Hao et al., 2017; Morid et al., 2006). Rigid model structures in both GCMs and  
69 RCMs cannot adaptively adjust to accommodate intrinsic data characteristics. Insufficient n  
70 onlinear processing capabilities in land surface models and statistical methods (including A  
71 RMA, ARIMA, and RF models) cannot capture complex feedback mechanisms and thresho  
72 ld effects(AghaKouchak et al., 2015). Additionally, there are difficulties in multi-scale infor  
73 mation integration and heterogeneous data fusion, particularly in land surface models and  
74 GCMs (Wood et al., 2016). High parameter sensitivity affects the robustness and generaliz  
75 ation capability of both physics-based and statistical models (including ARMA, ARIMA, a  
76 nd RF models) (Svoboda et al., 2002). Finally, trade-offs between computational efficiency  
77 and accuracy challenge the operational implementation requirements of RCMs and complex  
78 statistical models (Mo, 2008; Yuan & Quiring, 2017).

79 Recent advances in artificial intelligence and big data technologies have fundamentally  
80 transformed time series modeling and prediction across multiple fields (LeCun et al., 2015;  
81 Shlezinger et al., 2023). Deep learning methods demonstrate significant advantages in automatically  
82 capturing complex patterns and latent features without requiring pre-specified physical relationships,

83 possessing powerful nonlinear mapping and adaptive learning capabilities (Bengio et al., 2013;  
84 Schmidhuber, 2015). Long-Short-Term Memory (LSTM) networks have been successfully applied  
85 to various hydrological nonlinear sequence modeling tasks, including streamflow prediction, flood  
86 forecasting, and water level estimation, demonstrating superior predictive performance (Kratzert et  
87 al., 2018; Zhang et al., 2014). LSTM networks through their unique gate mechanisms and memory  
88 cell design effectively address gradient vanishing problems in traditional recurrent neural networks  
89 and exhibit excellent performance in capturing long-term dependency information (Greff et al.,  
90 2017). However, single deep learning architectures still have limitations when processing complex  
91 time series data, and multi-model ensemble and parallel architecture designs provide novel  
92 approaches for further enhancing prediction performance (Mosavi et al., 2018; Sit et al., 2020).

93 To enhance model capability for processing non-stationary complex sequences, signal  
94 decomposition algorithms for data preprocessing have become key strategies for improving time  
95 series prediction performance. Variational Mode Decomposition (VMD), an advanced adaptive  
96 signal decomposition technique proposed by Dragomiretskiy and Zosso in 2014, decomposes non-  
97 linear, non-stationary complex sequences into multiple Intrinsic Mode Functions (IMFs) with  
98 different center frequencies. Each IMF reflects the dynamic characteristics of the original sequence  
99 at specific frequency levels, possessing relatively independent frequency bandwidth and amplitude  
100 modulation properties (Dragomiretskiy & Zosso, 2014). Compared to traditional decomposition  
101 methods such as Empirical Mode Decomposition (EMD) and Ensemble EMD (EEMD), VMD is  
102 based on rigorous variational optimization theoretical frameworks, employs completely non-  
103 recursive decomposition models, effectively avoids mode mixing and end-effect problems, and  
104 possesses superior frequency separation effects and noise robustness.

105 In recent years, Transformer architectures have achieved major breakthroughs in time series  
106 prediction, particularly the informer model specifically optimized for long time series prediction  
107 tasks. Zhou proposed that informer reduces computational complexity from  $O(L^2)$  to  $O(L\log L)$   
108 through Probabilistic Sparse Self-attention mechanisms, combined with self-attention distillation  
109 operations that progressively compress sequence length layer by layer, significantly improving  
110 efficiency and accuracy in processing lengthy sequences (Zhou et al., 2021a). This innovative  
111 architecture provides novel technical pathways for capturing long-range temporal dependencies.

112 This study adopts the Daily Evapotranspiration Deficit Index (DEDI) as a drought monitoring  
113 indicator, constructed based on daily actual and potential evapotranspiration from ERA5 reanalysis  
114 data, which can effectively reflect the dynamic evolution processes of regional droughts (Hersbach  
115 et al., 2020; Zhang et al., 2022; Zuo et al., 2020). Building upon this foundation, we propose a novel  
116 drought prediction model integrating Variational Mode Decomposition, informer, and Long Short-  
117 Term Memory networks (VMD-informer-LSTM), which is expected to provide a high-accuracy,  
118 robust prediction framework for drought prediction applications by combining the technical  
119 advantages of variational optimization decomposition, probabilistic sparse attention mechanisms,  
120 and gated memory networks. Through a combination of multiscale feature decomposition and  
121 hybrid deep learning architectures, this method effectively handles the non-stationary characteristics  
122 of complex drought indices like DEDI, accurately capturing long-range climate trends and short-  
123 term fluctuations. This study significantly improved prediction accuracy and reliability of complex  
124 non-stationary drought time series and provided scientific foundations for regional water resource  
125 management and drought risk assessment (Pozzi et al., 2013; Willmott & Matsuura, 2005).

126 The technical approach includes: (1) utilizing VMD for adaptive modal decomposition of

127 original DEDI sequences, deconstructing complex nonlinear time series into multi-frequency scale  
128 IMF components to achieve structured extraction of multi-scale features (Dragomiretskiy & Zosso,  
129 2014; Johny et al., 2022); (2) constructing dual-branch parallel architecture of informer and LSTM,  
130 where informer efficiently captures global trends of long-range sequences through probabilistic  
131 sparse attention mechanisms, while LSTM precisely models local temporal dynamics through  
132 gating mechanisms (Zhou et al., 2021b); (3) fusing dual-source features through fully connected  
133 layers to form hybrid feature representations possessing both long-range dependency analysis  
134 capability and short-term fluctuation capture ability (Li et al., 2023; Zhang et al., 2019); (4) adopting  
135 a three-stage design of decomposition-parallelization-fusion to obtain final drought prediction  
136 results.

## 137 2 Study Area and data

### 138 2.1 Study Area

139 The Huaihe River Basin originates from the Tongbai Mountains in Nanyang City, Henan  
140 Province, China. It is located between 111°55'-121°20'E longitude and 30°55'-36°20'N latitude,  
141 covering approximately 270,000 km<sup>2</sup>. The basin is situated in China's north-south climate transition  
142 zone, with the area north of the Huaihe River belonging to the warm temperate zone and the area  
143 south of the river belonging to the northern subtropical zone (Yao et al., 2024). The annual mean  
144 temperature ranges from 11-16°C, with temperature variations increasing from north to south and  
145 from coastal to inland areas. The Huaihe River Basin receives a multi-year average precipitation of  
146 883 mm, with a spatial distribution characterized by higher precipitation in mountainous areas  
147 compared to plains, increased precipitation along the coast than inland, and a decreasing gradient  
148 from south to north. The multi-year average evaporation in the basin fluctuates between 650-1250  
149 mm, primarily concentrated during May-August, with an overall decreasing trend from south to  
150 north and from east to west. The studied region is shown in Fig. 1.

151 During the 62-year period from 1949 to 2010, the Huaihe River Basin experienced cumulative  
152 drought-affected areas of 167 million hectares, with disaster-affected areas of 87.3 million hectares,  
153 resulting in grain losses of 13.96 billion kg. On average, 2.698 million hectares of crops were  
154 affected by drought annually, with 1.408 million hectares suffering disaster-level impacts (Gao et  
155 al., 2015). Drought disasters have severely impacted industrial and agricultural production, urban  
156 and rural water supply security, and ecological environments within the basin, becoming one of the  
157 primary factors constraining rapid and sustainable socio-economic development in the region.  
158 Therefore, providing reliable drought prediction methods is of great significance for accurate  
159 drought forecasting and the scientific development of drought response strategies in the Huaihe  
160 River Basin.

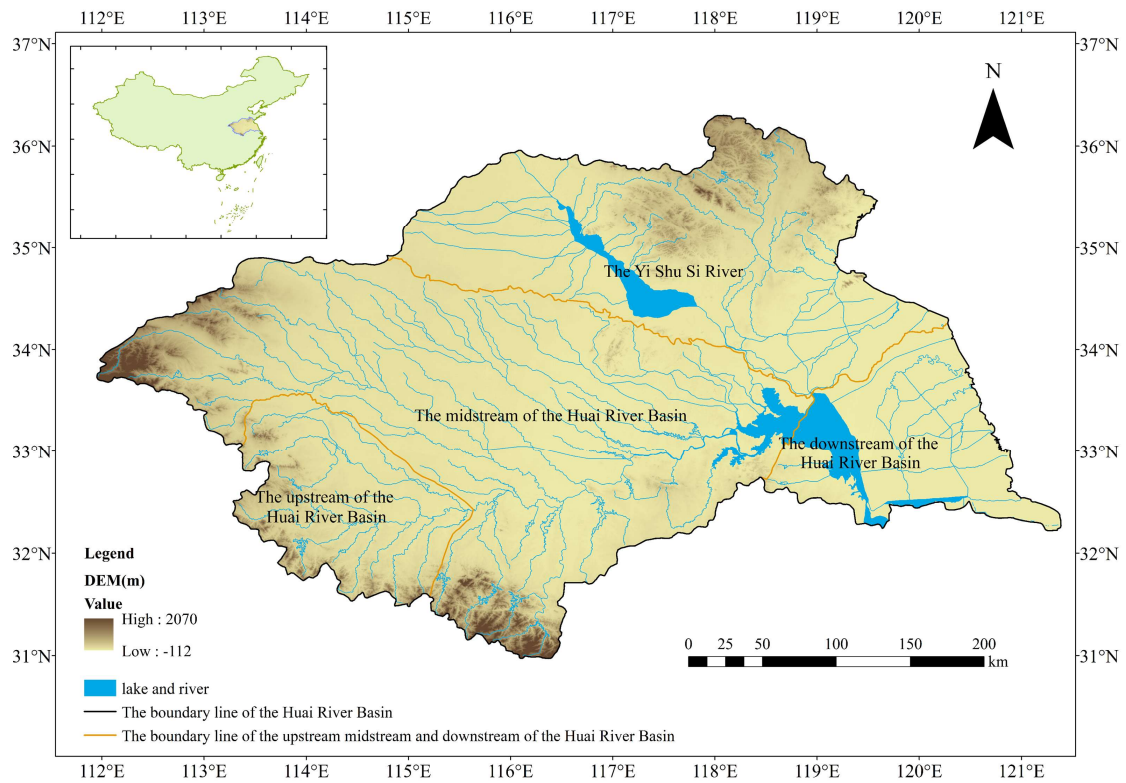


Figure 1 The study area of Huaihe river Basin

## 2.2 Data Sources

This study utilizes daily actual evapotranspiration, potential evapotranspiration, surface pressure, cloud cover, maximum temperature, mean temperature, wind speed, and precipitation data for the period 1980-2020, sourced from the fifth-generation high-resolution atmospheric reanalysis product (ECMWF Reanalysis v5, ERA5) developed by the European Centre for Medium-Range Weather Forecasts (ECMWF). ERA5 data are characterized by extensive coverage, long time series, and excellent spatio-temporal consistency. This makes them an optimal data choice for long-term and high-resolution analyses. To meet the specific spatial resolution requirements of this study, the downloaded ERA5 data were further subjected to interpolation processing. This converted them to a spatial resolution of  $0.25^\circ \times 0.25^\circ$  to more precisely match the spatial characteristics of the study region (Muñoz-Sabater et al., 2021). Land use data for 2005, 2010, 2015, and 2020 with a spatial resolution of 1 km were obtained from the Data Center for Resources and Environmental Sciences, Chinese Academy of Sciences (<https://www.resdc.cn/>).

## 3. Methods

### 3.1 DEDI Index

The Daily Evapotranspiration Deficit Index (DEDI) is a daily drought index constructed based on daily evapotranspiration as well as potential evapotranspiration for monitoring and predicting regional drought events (Zhang et al., 2022). This index is calculated based on ERA5 data provided by ECMWF.

The DEDI is calculated as follows:

$$DEDI_i = \frac{D_i - D_{AVE}}{D_{STU}} \quad (1)$$

$$D_i = AET_i - PET_i \quad (2)$$

183 where  $i$  represents time,  $AET_i$  represents the actual evapotranspiration on day  $i$  (units:  
 184 mm/day),  $PET_i$  represents the potential evapotranspiration on day  $i$  (units: mm/day),  $D_i$   
 185 represents the evapotranspiration deficit between AET and PET on day  $i$ , and  $D_{AVE}$  and  $D_{STU}$  are  
 186 the multi-year climatological mean and standard deviation, respectively (Zuo et al., 2020).

## 187 3.2 VMD

188 Variational Mode Decomposition (VMD) was proposed by Konstantin Dragomiretskiy  
 189 (Dragomiretskiy & Zosso, 2014) as a signal processing method designed to effectively overcome  
 190 mode mixing and end effect problems existing in Empirical Mode Decomposition (EMD). Unlike  
 191 the recursive decomposition principle of EMD, VMD determines the central frequency and  
 192 bandwidth of each mode component. This is done by constructing and solving the optimal solution  
 193 to a variational model. This represents a completely non-recursive decomposition model. This  
 194 method searches for a set of mode components and their corresponding center frequencies through  
 195 an iterative search. This ensures that each mode maintains smoothness after demodulation to  
 196 baseband.

197 The adaptivity of VMD is reflected in its ability to automatically determine the number of  
 198 modes decompositions according to signal characteristics and adaptably match the optimal center  
 199 frequency and finite bandwidth for each mode, thereby achieving effective separation of Intrinsic  
 200 Mode Functions (IMFs) and frequency domain partitioning of signals. Experimental results  
 201 demonstrate that VMD exhibits strong robustness in sampling and noise aspects, is capable of  
 202 reducing the non-stationarity of time series with high complexity and strong non-linearity and  
 203 decomposing them into multiple sub-sequences with different frequency scales that are relatively  
 204 stationary, making it particularly suitable for non-stationary signal processing.

205 VMD decomposes time series into simple high-frequency and low-frequency intrinsic mode  
 206 functions through optimization processes, improving signal processing stability and accuracy. This  
 207 method is not only theoretically innovative but also demonstrates superior performance in practical  
 208 applications, providing an effective tool for non-stationary signal analysis. Research by Zhao et al.  
 209 (2023) further proved VMD's excellent performance in handling boundary effects by adjusting  
 210 parameters (such as decomposition levels, quadratic penalty terms, etc.) to effectively control  
 211 deviations in decomposition results, thereby improving model adaptability (Zhang et al., 2023; Zhao  
 212 et al., 2023).

213 In this study, two key parameters of the Variational Mode Decomposition (VMD) need to be  
 214 predefined: the penalty factor  $\alpha$  (bandwidth constraint parameter) and the number of modes  $K$  (i.e.,  
 215 the number of intrinsic mode functions, IMFs). The penalty factor  $\alpha$  is empirically determined based  
 216 on the length of the time series, with its value ranging from 1.5 to 2.0 times the sample length,  
 217 aiming to balance frequency band separation and decomposition stability. When  $\alpha$  is relatively small,  
 218 the bandwidth of each IMF becomes wider, which may lead to spectral overlap between different  
 219 modes and thus reduce the physical interpretability of the decomposition results; whereas when  $\alpha$  is  
 220 excessively large, the bandwidth is overly constrained, making the decomposition more sensitive to  
 221 noise. In this study,  $\alpha$  is finally set to 1.75 times the sample length. In addition, the number of modes  
 222  $K$  is determined based on the frequency distribution characteristics of the decomposed signal and

223 preliminary experimental results. When K is less than 7, certain IMF components exhibit significant  
 224 spectral mixing, making it difficult to effectively separate signals at different time scales; when K  
 225 exceeds 7, the center frequencies of adjacent IMFs become too close and the energy distribution  
 226 tends to be dispersed, resulting in redundant or noise-dominated modes and thus reducing the  
 227 stability and physical interpretability of the decomposition. Therefore, K is uniformly set to 7 in this  
 228 study to ensure effective separation of the dominant frequency components of the original DEDI  
 229 series while avoiding redundancy caused by over-decomposition. Preliminary experiments  
 230 conducted on several representative grid points indicate that this parameter combination yields  
 231 stable decomposition results and satisfactory predictive performance. To maintain methodological  
 232 consistency and avoid potential spatial overfitting, the same VMD parameter settings are applied  
 233 uniformly across all grid points in the study area.

234 Assuming the original signal  $f$  is decomposed into  $k$  components, ensuring that the decomposed  
 235 sequences are modal components with finite bandwidth and center frequencies, while minimizing  
 236 the sum of estimated bandwidths of all modes, with the constraint that the sum of all modes equals  
 237 the original signal, the VMD constrained variational model is as follows:

$$\min_{\{u_k, \omega_k\}} \left\{ \sum_{k=1}^K \left\| \partial_t \left[ \left( \delta(t) + \frac{j}{\pi t} \right) * u_k(t) \right] e^{-j\omega_k t} \right\|_2^2 \right\} \quad (3)$$

$$\text{s. t. } \sum_k u_k = f(t) \quad (4)$$

$$u_k = \{u_1, u_2, \dots, u_k\} \quad (5)$$

$$\omega_k = \{\omega_1, \omega_2, \dots, \omega_k\} \quad (6)$$

238 where  $f(t)$  represents the original data;  $K$  represents the number of modal components;  
 239  $\delta(t)$  represents the Dirac function;  $*$  represents convolution operation;  $\partial_t$  is the partial derivative  
 240 operator;  $\{u_k\}$  represents the  $k$ -th component function obtained through calculation;  $\{\omega_k\}$   
 241 represents the center frequency of the  $k$ -th component obtained through calculation.

242 The augmented LaGrange is introduced to solve this constrained optimization problem:

$$\begin{aligned} L(\{u_k\}, \{\omega_k\}, \lambda) = & \alpha \sum_k \left\| \partial_t \left[ \left( \delta(t) + \frac{j}{\pi t} \right) * u_k(t) \right] e^{-j\omega_k t} \right\|_2^2 \\ & + \left\| f(t) - \sum_k u_k(t) \right\|_2^2 + \left\langle \lambda(t), f(t) - \sum_k u_k(t) \right\rangle \end{aligned} \quad (7)$$

243 where  $\alpha$  represents the penalty factor;  $\lambda(t)$  represents the Lagrange multiplier.

244 The alternating direction method of multipliers (ADMM) is used to find the saddle point of the  
 245 augmented LaGrange. In the frequency domain, the updates are:

$$\hat{u}_k^{n+1}(\omega) = \frac{\hat{f}(\omega) - \sum_{i \neq k}^k \hat{u}_i^{n+1}(\omega) + \frac{\hat{\lambda}^n(\omega)}{2}}{1 + 2\alpha(\omega - \omega_k^n)^2} \quad (8)$$

$$\omega_k^{n+1} = \frac{\int_0^\infty \omega |u_k^{n+1}(\omega)| d\omega}{\int_0^\infty |u_k^{n+1}(\omega)| d\omega} \quad (9)$$

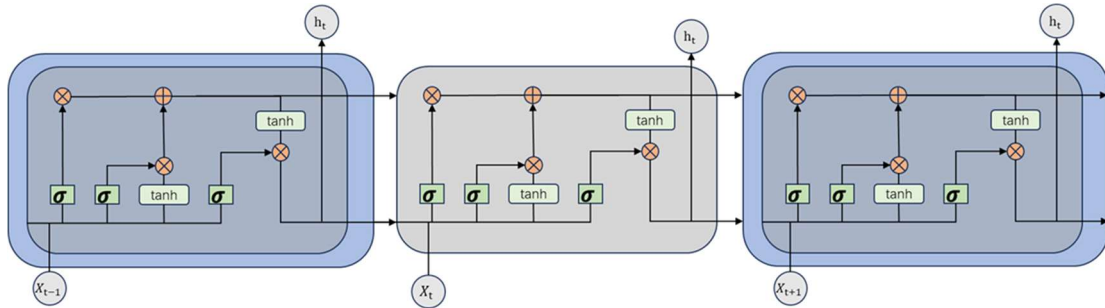
$$\hat{\lambda}^{n+1}(\omega) \leftarrow \hat{\lambda}^n(\omega) + \pi \left[ \hat{f}(\omega) - \sum_{i \neq k} \hat{u}_i^{n+1}(\omega) \right] \quad (10)$$

246 where  $\gamma$  represents noise tolerance; the  $\hat{u}_k^{n+1}(\omega)$  represent Wiener filtering residuals;  $\hat{u}_i(\omega)$ ,  
 247 and  $\hat{\lambda}^n(\omega)$  represent the Fourier transforms of  $u(t)$  and  $\lambda(t)$ , respectively.

### 248 3.3 LSTM

249 The Long-Short-Term Memory (LSTM) models are a special type of Recurrent Neural  
 250 Network (RNN) variant that addresses the gradient vanishing problem in RNN processing of long  
 251 sequence data by introducing memory cells (Cell States), specifically designed for processing time  
 252 series data (Hochreiter & Schmidhuber, 1997). When recording long sequence data, RNN  
 253 experiences gradient vanishing or exploding due to continuous information accumulation, making  
 254 it difficult for the network to learn long-term dependencies, ultimately affecting the model's accurate  
 255 capture of trends and periodicity in time series data (Jaseena & Kovoor, 2022).

256 LSTM aims to solve the gradient-vanishing or exploding problems encountered by traditional  
 257 RNN when processing long sequence data. This is done mainly through gate mechanisms regulating  
 258 information flow. The LSTM model consists of four interacting layers: input gate, forget gate, cell  
 259 state gate, and output gate. It is shown in Fig. 2 below.



260  
261 Figure 2 The construction of LSTM

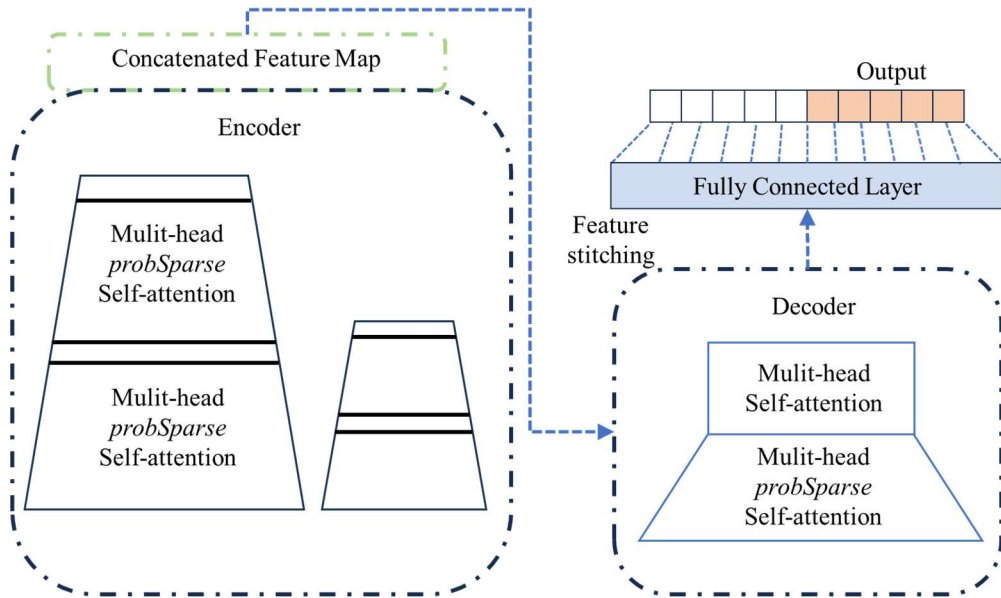
### 262 3.4 informer

263 informer is an improved and optimized version based on Transformer, specifically designed to  
 264 enhance the speed and efficiency of processing long sequences and optimized for long-term time  
 265 series prediction tasks (Zhou et al., 2021b). Transformer captures relationships between different  
 266 positions in sequences through Self-Attention mechanisms. However, Transformer encounters  
 267 difficulties when processing long time series data because its computational complexity grows  
 268 quadratically with sequence length, becoming very slow or even unprocessable when dealing with  
 269 very long time series.

270 informer proposes ProbSparse Self-attention to filter critical queries and reduce computational  
 271 complexity, and introduces Self-attention Distilling to reduce dimensions and network parameters  
 272 (Vaswani et al., 2017). As shown in Fig. 3, the informer architecture consists of an encoder-decoder  
 273 structure. Input sequences first undergo convolutional encoding and positional embedding before  
 274 being fed into the encoder; the encoder utilizes multi-layer probabilistic sparse self-attention and  
 275 distillation operations to extract key information, outputting encoded features. The decoder then  
 276 directly generates long sequence predictions under masked self-attention and cross-attention,  
 277 followed by fully connected layers mapping to final values.

278 For long sequence prediction, the informer has three advantages: 1. Probabilistic sparse self-  
 279 attention reduces time complexity from  $O(L^2)$  to  $O(L \log L)$ , significantly reducing computational  
 280 overhead; 2. Self-attention distillation progressively compresses the sequence length layer by layer,

281 simultaneously reducing computation and memory requirements; 3. Generative decoding outputs  
 282 complete future sequences at once, avoiding error accumulation caused by step-by-step  
 283 extrapolation.



284  
 285

Figure 3 The construction of the informer

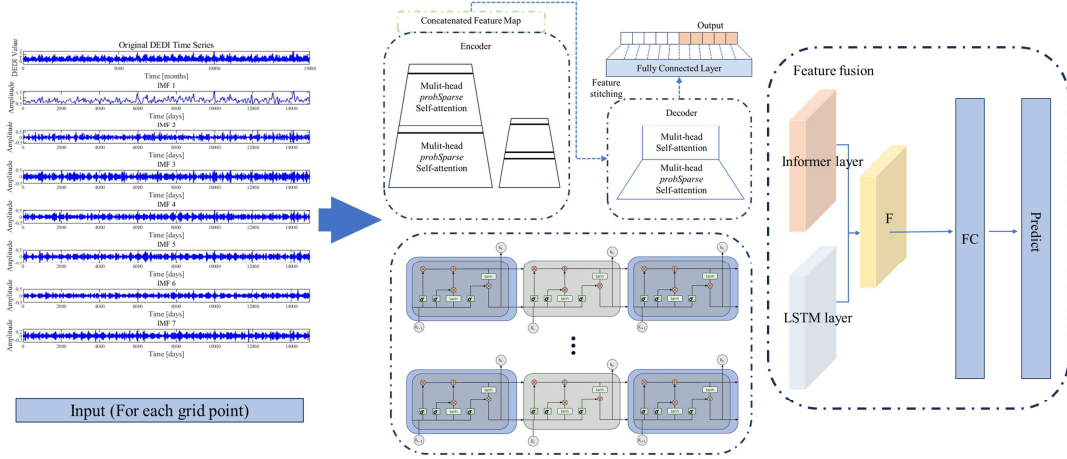
### 286 3.5 VMD-informer-LSTM

287 The VMD-informer-LSTM model employs Variational Mode Decomposition (VMD) to  
 288 deconstruct DEDI time series into multi-frequency scale Intrinsic Mode Functions (IMFs),  
 289 achieving the structured extraction of multi-scale features. Based on this foundation, it constructs a  
 290 dual-branch parallel architecture of informer and LSTM, where informer efficiently captures global  
 291 trends of long-range sequences through probabilistic sparse attention mechanisms, while LSTM  
 292 precisely models local temporal dynamics through gate mechanisms. Finally, dual-source features  
 293 are fused through fully connected layers to form hybrid feature representations possessing both  
 294 long-range dependency analysis capability and short-term fluctuation capture ability. This model  
 295 significantly improves prediction accuracy and reliability for complex time series data through a  
 296 three-stage design of decomposition-parallelization-fusion, providing an innovative solution for  
 297 time series prediction tasks. The construction of VMD-informer-LSTM is shown in Fig. 4 below.

298 Building upon this foundation, in order to ensure the standardization of the model training  
 299 process and the reproducibility of the results, this study further establishes a unified design for  
 300 dataset partitioning and hyperparameter optimization procedures. For the DEDI time-series data at  
 301 each grid point, the dataset is strictly divided in chronological order using a forward-splitting  
 302 strategy to prevent any potential leakage of future information. Specifically, the training period  
 303 spans from January 1, 1984 to July 3, 2024, while the testing period covers July 4, 2024 to December  
 304 31, 2024, which is used to evaluate the model's predictive performance on unseen data over the  
 305 subsequent 180-day forecasting horizon. It should be noted that the 180-day prediction in this study  
 306 does not correspond to traditional deterministic weather forecasting, but rather focuses on predicting  
 307 the evolution of drought states.

308 Regarding hyperparameter configuration, this study adopts the Bayesian Optimization method  
 309 to automatically search for key hyperparameters (including hidden layer dimension, learning rate,

310 and batch size) within a predefined parameter search space. Each candidate parameter combination  
 311 is evaluated based on its predictive performance on the validation set, with the minimization of  
 312 validation error serving as the optimization objective function. The optimal parameter combination  
 313 is then selected for the final model training and testing evaluation. Through the design of the above  
 314 training strategy and hyperparameter optimization procedure, the experimental process ensures  
 315 methodological rigor, stability of results, and reproducibility of the research.



316  
 317

Figure 4 The construction of VMD-informer-LSTM

### 318 3.5 Shapley Additive Explanations

319 Since machine learning models are “black-box” models, although they can provide efficient  
 320 predictions, their internal decision-making processes are complex and difficult to intuitively  
 321 understand and explain. This may affect result analyses in the field of raster data, which require  
 322 transparency and interpretability. To overcome such problems, SHAP values are introduced as an  
 323 interpretive method. The SHAP value method was proposed by Lundberg et al (Lundberg & Lee,  
 324 2017). In 2017, it is a method based on cooperative game theory that quantifies the contribution of  
 325 driving factors to model prediction results. By calculating the marginal contributions of each factor  
 326 to the model output under different combinations, it measures their importance in the overall  
 327 prediction results. This helps us understand how the model makes decisions. The positive or  
 328 negative values of SHAP indicate promotion or inhibition of prediction results. The absolute value  
 329 reflects the degree of influence of the factor on the model prediction results. The larger the absolute  
 330 value, the greater the influence of the factor on model prediction results (Wang et al., 2024). The  
 331 formula is as follows:

$$\phi_i = \sum_{S \in N \setminus \{i\}} \frac{|S|! (|N| - |S| - 1)!}{|N|!} [f(S \cup \{i\}) - f(S)] \quad (11)$$

332 In the formula,  $\phi_i$  represents the SHAP value for feature  $i$ ;  $N$  is the set of all features;  $S$  is a  
 333 subset of features, excluding feature  $i$ ;  $f(S)$  is the model output using only the feature subset  $S$  for  
 334 prediction;  $(f(S \cup \{i\}))$  is the predicted value after adding feature  $i$  to the featured subset  $S$ .

### 335 3.6 Evaluation Metrics

336 The coefficient of determination ( $R^2$ ) measures the proportion of variance in the dependent  
 337 variable that is derived from the independent variable, ranging from 0 to 1, where values closer to

338 1 indicate better model performance (Nash & Sutcliffe, 1970). The root mean square error (RMSE)  
 339 quantifies the average magnitude of prediction errors, providing a measure of how well the model  
 340 predicts actual values, with lower values indicating better accuracy (Willmott & Matsuura, 2005).  
 341 Mean absolute error (MAE) represents the average absolute difference between predicted and  
 342 observed values, offering a linear score that is less sensitive to outliers than RMSE. The range of  
 343 mean absolute percentage error (MAPE) is  $[0, +\infty]$ . A MAPE of 0% indicates a perfect model, while  
 344 a MAPE greater than 100% suggests a poor model (Myttenaere et al., 2016).

345 The mathematical expressions for these metrics appear as follows:

$$R^2 = 1 - \frac{SSE}{SST} = 1 - \frac{\sum_{i=1}^N (y_{obs} - y_{pred})^2}{\sum_{i=1}^N \Sigma (y_{obs} - \bar{y}_{obs})^2} \quad (12)$$

$$RMSE = \sqrt{\frac{1}{N} \sum_{i=1}^N (y_{obs} - y_{pred})^2} \quad (13)$$

$$MAE = \frac{1}{N} \sum_{i=1}^N |y_{obs} - y_{pred}| \quad (14)$$

$$MAPE = \frac{1}{N} \sum_{i=1}^N abs\left(\frac{y_{obs} - y_{pred}}{y_{obs}}\right) \quad (15)$$

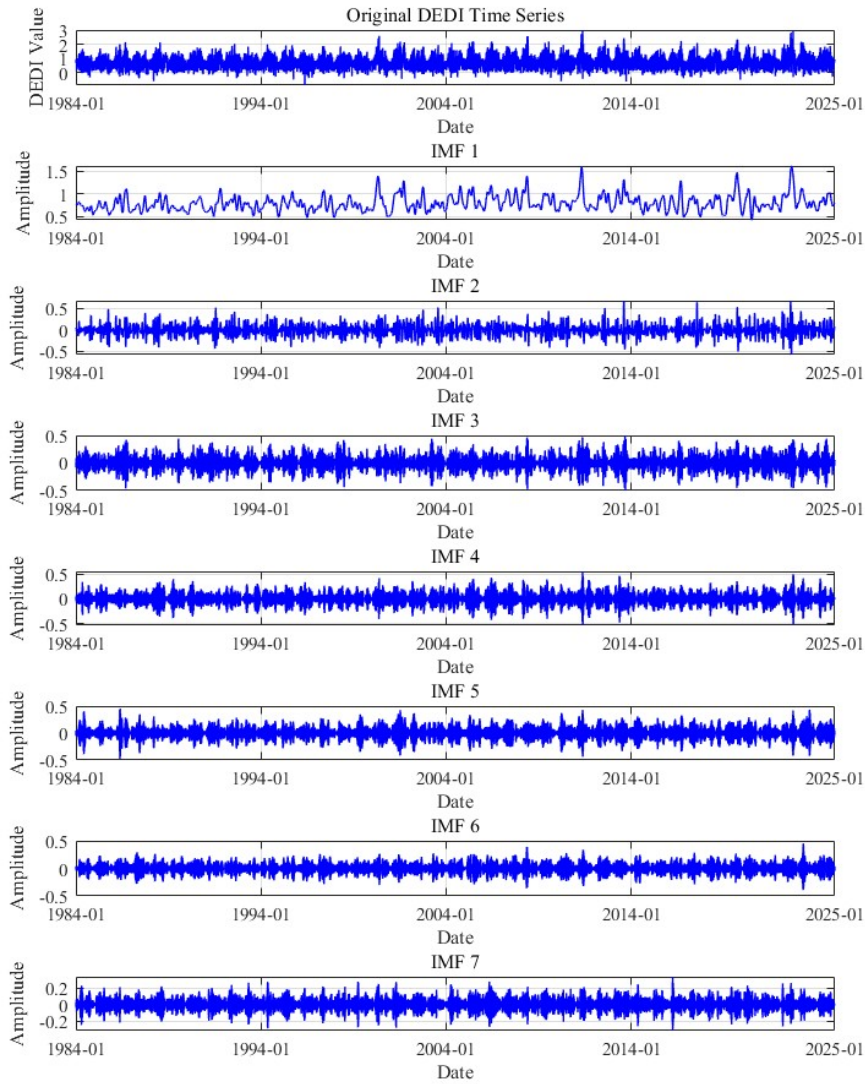
346 where  $y_{obs}$  represents observed values,  $y_{pred}$  represents predicted values,  $\bar{y}_{obs}$  is the mean of  
 347 observed values, and  $n$  is the number of observations.

348

## 349 4. Results

### 350 4.1 VMD Decomposition Results

351 In this study, we systematically selected 108 grid points distributed across the Huaihe River  
 352 Basin and performed VMD analysis of their corresponding daily DEDI time series data spanning  
 353 1980-2020. Fig. 5 provides a comprehensive visual representation of the decomposed sub-sequences  
 354 of DEDI data for a certain representative grid cell in the Huaihe River Basin. As illustrated in Fig.  
 355 5, the daily DEDI values for a representative grid cell in the Huaihe River Basin exhibit substantial  
 356 positive and negative fluctuations, with considerable variance between maximum and minimum  
 357 values. These pronounced oscillations present significant challenges in capturing essential features  
 358 during the prediction process, as the complex, non-stationary nature of the original signal obscures  
 359 the underlying patterns and trends. The VMD algorithm successfully decomposes the complex, non-  
 360 linear DEDI time series into multiple distinct IMFs, each characterized by specific frequency bands  
 361 and temporal scales. These decomposed components reveal multi-scale variability patterns ranging  
 362 from high-frequency short-term fluctuations to low-frequency long-term trends, facilitating more  
 363 effective feature extraction and modeling processes. VMD technology demonstrates superior  
 364 capability in accurately tracking changes in signal frequency components and effectively revealing  
 365 the intrinsic and dynamic characteristics of time series, thereby substantially enhancing prediction  
 366 accuracy and reliability.



367

368 Figure 5 The daily DEDI values of a certain grid in the Huaihe River Basin are decomposed into 7  
 369 sub - sequence through variational mode decomposition (VMD).

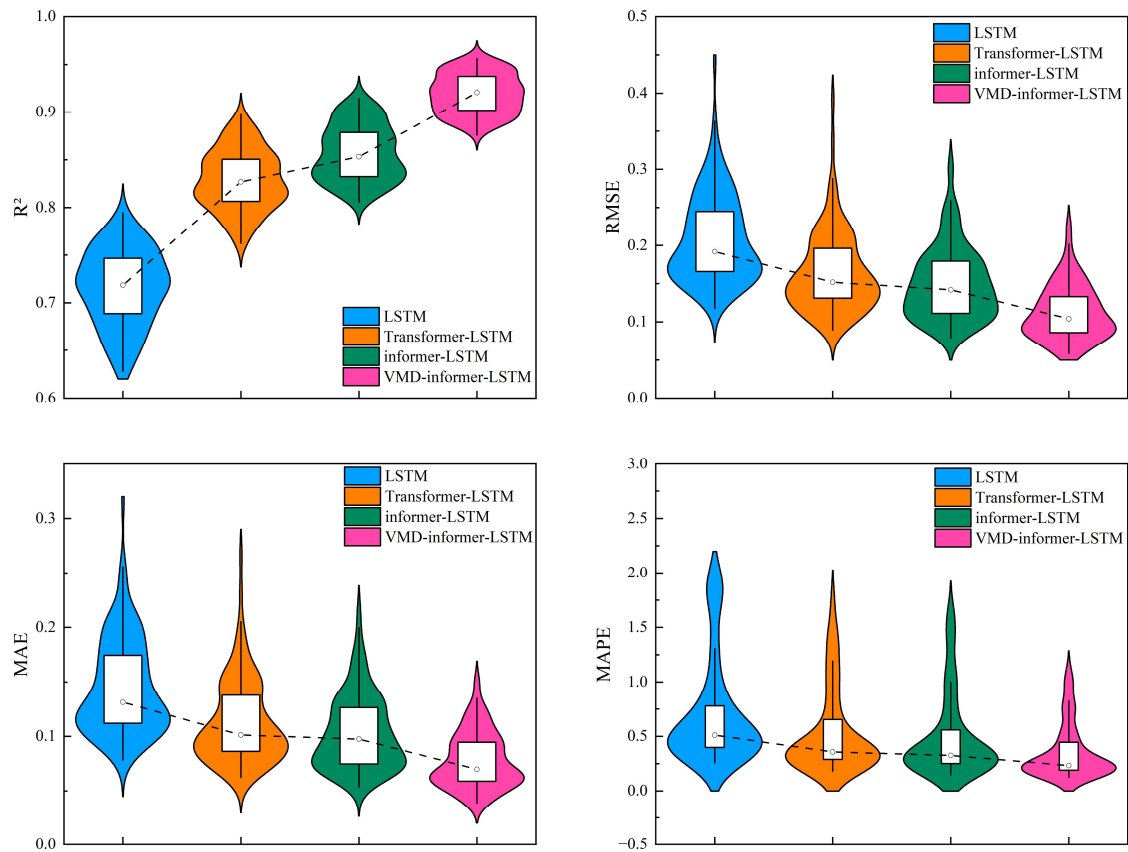
## 370 4.2 Model Prediction Performance Evaluation

371 To evaluate the performance of the proposed VMD-informer-LSTM model, we performed  
 372 extensive comparative experiments involving four distinct modeling approaches: the proposed  
 373 VMD-informer-LSTM model, the informer-LSTM model, the Transformer-LSTM model, and the  
 374 standalone LSTM model. The evaluation of each model's performance was based on four widely  
 375 used statistical metrics for time series prediction evaluation. From Table 1, it can be seen that the  
 376 VMD-informer-LSTM model performs the best in terms of predictive performance, with  $R^2$ , RMSE,  
 377 MAE, and MAPE reaching 0.9191, 0.1122, 0.0778, and 0.4056, respectively. In contrast, the  
 378 informer-LSTM model without VMD decomposition has  $R^2$ , RMSE, MAE, and MAPE of 0.8570,  
 379 0.1498, 0.1031, and 0.5330, respectively. After calculation, VMD decomposition improves  $R^2$ ,  
 380 RMSE, MAE, and MAPE by 7.25%, 25.10%, 24.54%, and 23.90%, respectively. Furthermore, the  
 381 traditional LSTM model shows relatively low predictive accuracy with four evaluation metrics of  
 382  $R^2=0.7156$ ,  $RMSE=0.2087$ ,  $MAE=0.1454$ , and  $MAPE=0.8254$ . The Transformer-LSTM model  
 383 achieves  $R^2$ , RMSE, MAE, and MAPE of 0.8286, 0.1641, 0.1130, and 0.6266, respectively. This,

384 although better than the basic LSTM model, is still not as good as the informer-LSTM model, let  
 385 alone the VMD-informer-LSTM model. In summary, by comparing the predictive performance of  
 386 the four models, it is evident that the VMD-informer-LSTM model has an advantage in time series  
 387 prediction tasks. Especially after the introduction of VMD decomposition, its performance has  
 388 significantly improved, further verifying the effectiveness of VMD decomposition in enhancing  
 389 model predictive accuracy.

390 Table 1 Overall average evaluation indicators of various models within the Huaihe River Basin

| Indicator | LSTM   | Transformer-LSTM | informer-LSTM | VMD-informer-LSTM |
|-----------|--------|------------------|---------------|-------------------|
| $R^2$     | 0.7156 | 0.8286           | 0.8570        | 0.9191            |
| RMSE      | 0.2087 | 0.1641           | 0.1498        | 0.1122            |
| MAE       | 0.1454 | 0.1130           | 0.1031        | 0.0778            |
| MAPE      | 0.8254 | 0.6266           | 0.5330        | 0.4056            |



391  
 392 Figure 6 Violin-box plots of evaluation indicators for different models in the Huaihe River Basin

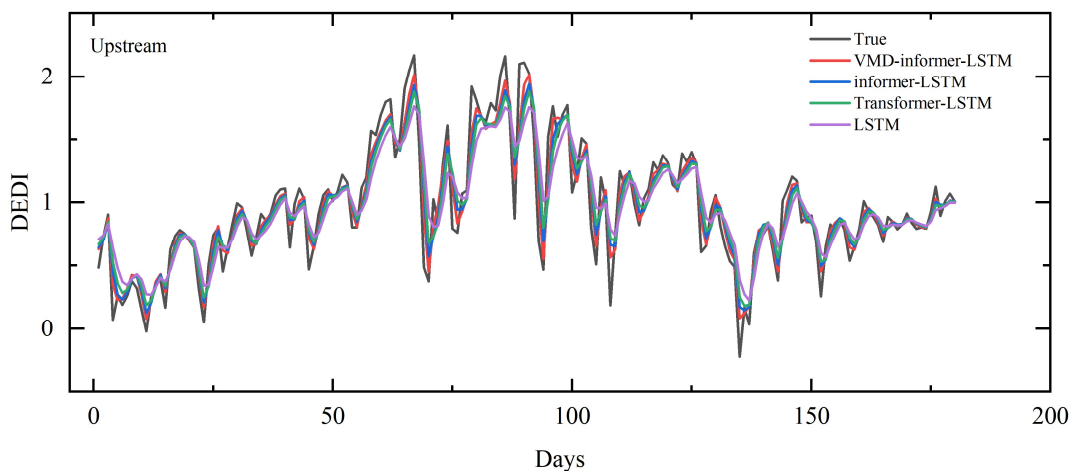
393 Fig. 6 presents violin plots illustrating the distribution of evaluation metrics across all 108 grid  
 394 points in the Huaihe River Basin. This provides insights into model performance variability and  
 395 consistency. Violin plots reveal important patterns. The VMD-informer-LSTM model demonstrates  
 396 the most concentrated distribution around optimal values, with  $R^2$  distributions tightly clustered near  
 397 0.92-0.95, indicating consistent and high performance across diverse geographical locations. Error  
 398 metric distributions (RMSE, MAE and MAPE) show the VMD-informer-LSTM model has the  
 399 narrowest spread and the lowest median values, suggesting robust prediction accuracy with minimal  
 400 spatial variability.

401 The RMSE distributions demonstrate a clear monotonic improvement from LSTM (median:

402 0.2087) through Transformer-LSTM (0.1641), informer-LSTM (0.1498) to VMD-informer-LSTM  
 403 (0.1122), with progressively narrower interquartile ranges and fewer outliers. The VMD-informer-  
 404 LSTM model exhibits the most concentrated distribution with minimal dispersion (IQR: 0.05),  
 405 indicating superior prediction accuracy and enhanced stability across diverse geographical locations.  
 406 This concentrated performance distribution reflects the effectiveness of combining VMD  
 407 decomposition with hybrid deep learning architectures for robust drought prediction.

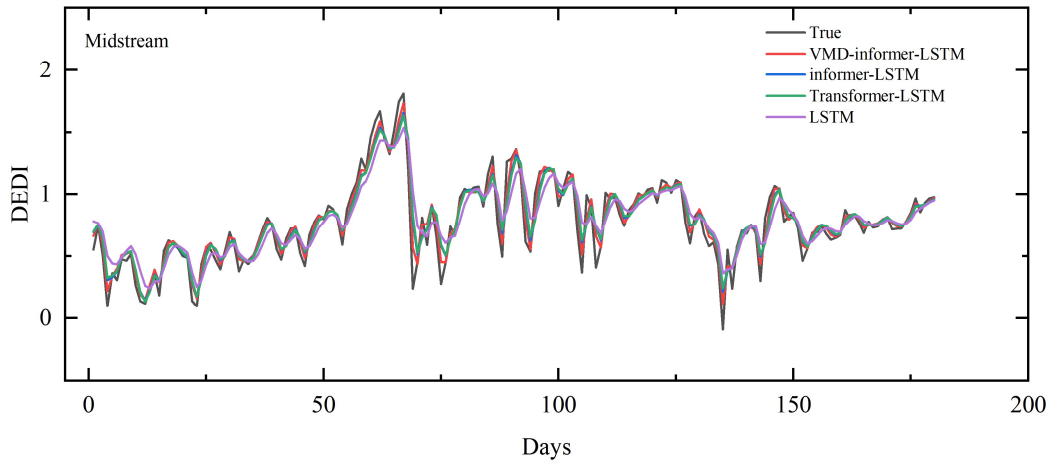
408 Comparing the four models, the VMD-informer-LSTM model consistently outperforms the  
 409 other three, with spatially averaged performance metrics across all 108 grid points in the Huaihe  
 410 River Basin, including an  $R^2$  of 0.9191, RMSE of 0.1122, MAE of 0.0778, and MAPE of 0.4056.  
 411 The informer-LSTM model without VMD decomposition has spatially averaged metrics across all  
 412 grid points of  $R^2 = 0.8570$ , RMSE = 0.1498, MAE = 0.1031, and MAPE = 0.5330. The Transformer-  
 413 LSTM model achieves spatially averaged metrics of  $R^2 = 0.8286$ , RMSE = 0.1641, MAE = 0.1130,  
 414 and MAPE = 0.6266, while the basic LSTM model shows the lowest performance, with spatially  
 415 averaged metrics of  $R^2 = 0.7156$ , RMSE = 0.2087, MAE = 0.1454, and MAPE = 0.8254.

416 The performance improvement from LSTM to Transformer-LSTM to informer-LSTM is  
 417 evident, with each model showing better median values and reduced spread in the error metrics  
 418 compared to the previous one. However, the VMD-informer-LSTM model stands out with the most  
 419 significant enhancements in both median performance and reduced variance across all metrics. This  
 420 indicates that the integration of VMD decomposition with the informer-LSTM architecture provides  
 421 the most substantial benefits in terms of prediction accuracy and consistency.



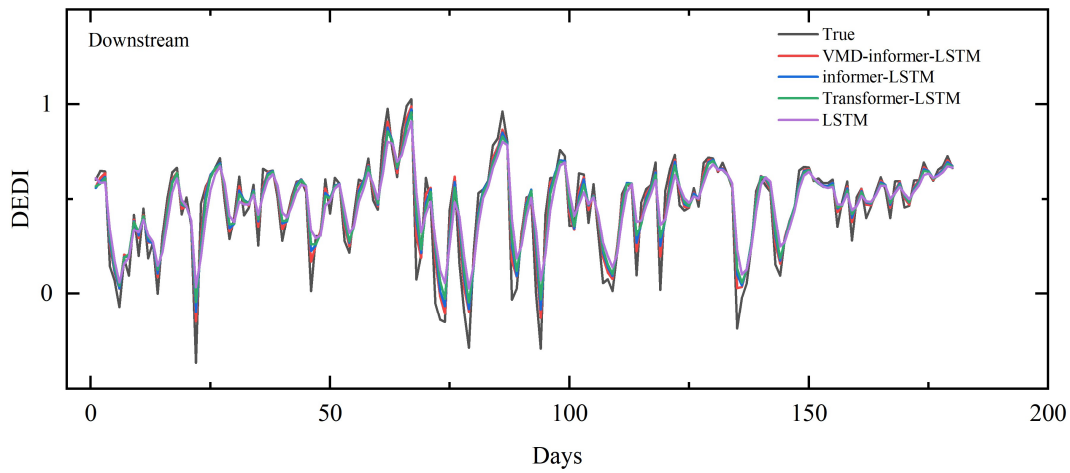
422  
 423

(a)



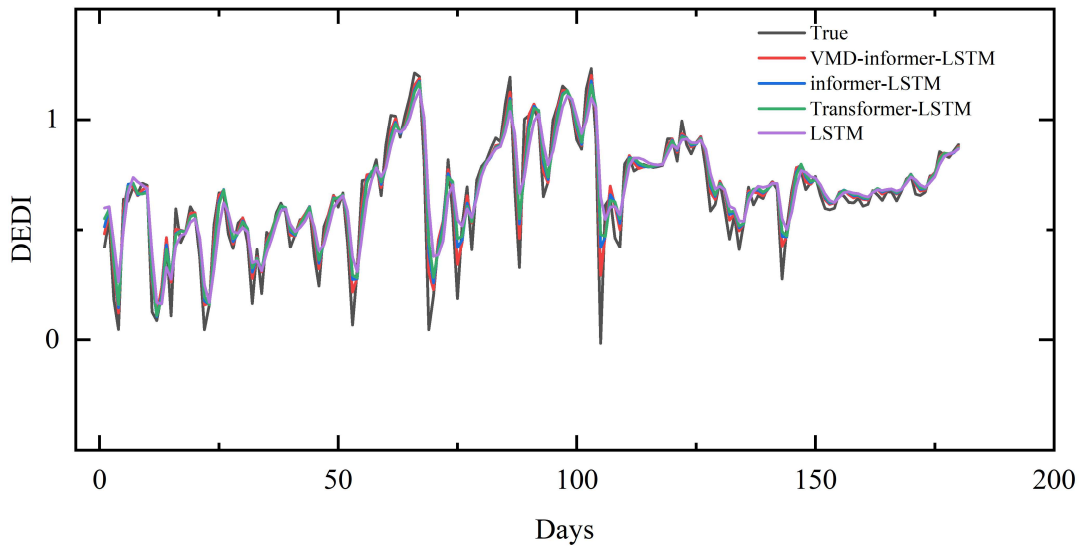
424  
425

(b)



426  
427

(c)



428  
429

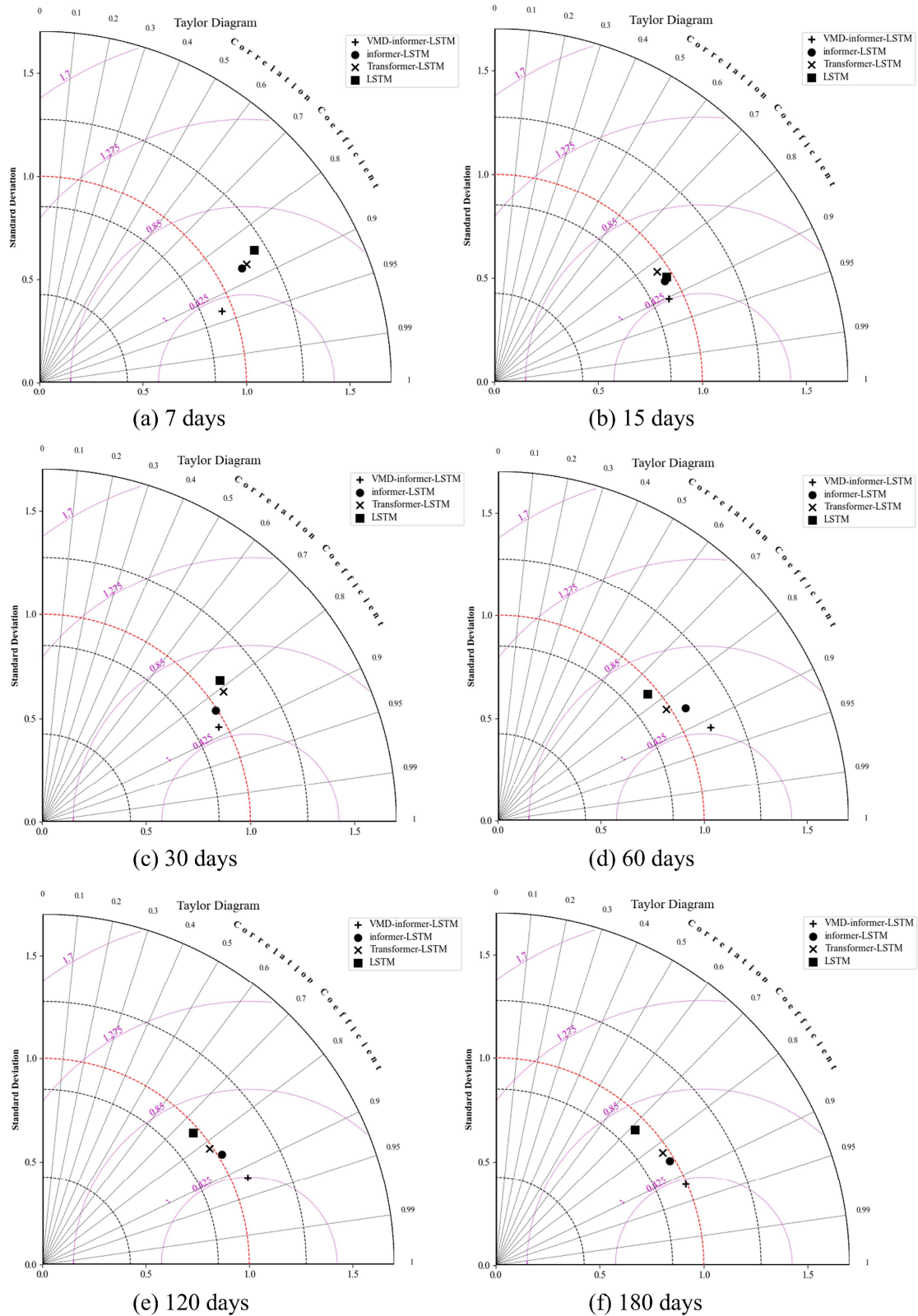
(d)

Figure 7 Line charts of different models' 180 - day predictions in four Huaihe River Basin  
Regions: (a) Upstream; (b) Midstream; (c) Downstream; (d) Yi Shu Si River

430  
431

432 Fig. S5 and Fig. 7 show scatter plots and line charts of different models' 180-day predictions  
433 in different Huaihe River Basin regions. As illustrated in Fig. S5, LSTM yields the lowest  $R^2$  values  
434 (0.76–0.78) across all subplots and is therefore the poorest performer; its scatter points visibly  
435 diverge from the 1:1 line, reflecting the largest prediction errors. Although informer-LSTM is less  
436 accurate than VMD-informer-LSTM, it maintains a stable  $R^2$  of about 0.89, and the scatter deviation  
437 is markedly smaller than those of Transformer-LSTM and LSTM.

438 Fig. 7 further indicates that all four models successfully capture the overall drought trend, yet  
439 differ in precision. When the line plots are examined in conjunction, it becomes clear that VMD-  
440 informer-LSTM outperforms the other three models, delivering superior agreement between  
441 simulated and ERA5 reanalysis values, higher prediction accuracy, and the best overall performance.  
442 informer-LSTM and Transformer-LSTM rank next, whereas LSTM only roughly reproduces the  
443 drought trend and performs poorly at predicting extremes, resulting in the lowest predictive  
444 capability.



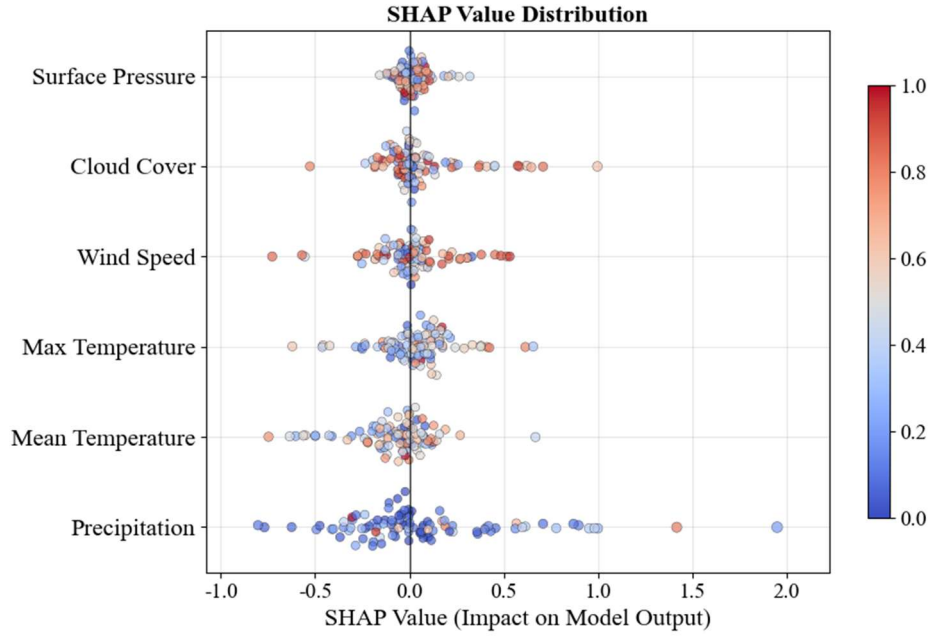
445  
 446 Figure 8 Taylor diagrams comparing the performance of different models for DEDI prediction in  
 447 the Huaihe River Basin at different lead times: (a) 7 days; (b) 15 days; (c) 30 days; (d) 60 days; (e)  
 448 120 days; (f) 180 days.

449 Fig. 8 presents Taylor diagrams that evaluate the predictive performance of various models  
 450 across different lead times: (a) 7 days, (b) 15 days, (c) 30 days, (d) 60 days, (e) 120 days, and (f)

451 180 days. These diagrams provide a comprehensive assessment by integrating standard deviation  
452 and correlation coefficients from the ERA5 reanalysis data. The VMD-informer-LSTM model  
453 consistently shows superior predictive accuracy across all lead times, with its predictions closely  
454 aligned with the ERA5 reanalysis data, particularly in the upper, middle, and lower regions of the  
455 Huaihe River Basin and the Yi Shu Si River regions. At short lead times (7 and 15 days), all models  
456 perform relatively well, but the VMD-informer-LSTM model slightly outperforms the others. As  
457 the lead time extends to 30 and 60 days, the VMD-informer-LSTM model maintains high accuracy  
458 while other models show performance degradation, indicating a reduced ability to capture the  
459 underlying data patterns effectively. At long lead times (120 and 180 days), the VMD-informer-  
460 LSTM model's advantage becomes more pronounced, with its predictions remaining significantly  
461 closer to the ERA5 reanalysis data than other models, which exhibit more noticeable divergence.  
462 This suggests that the VMD-informer-LSTM model is better equipped to handle the increased  
463 uncertainty and complexity associated with long-term predictions, highlighting its robustness and  
464 reliability in predictive tasks, especially crucial in drought forecasting where lead time is a critical  
465 factor.

### 466 4.3 Model Influencing Factor Analysis

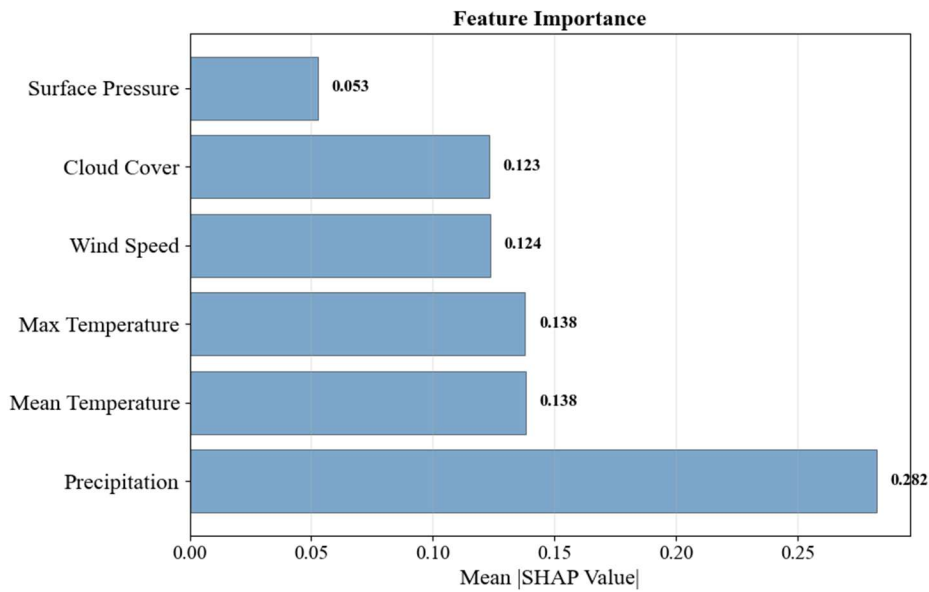
467 Fig. 9a presents a comprehensive SHAP value distribution analysis revealing the complex,  
468 non-linear relationships between meteorological variables and drought prediction outcomes.  
469 Precipitation emerges as the dominant predictor with predominantly positive SHAP contributions,  
470 indicating its critical role in alleviating drought conditions through direct water supply augmentation.  
471 However, the wide distribution of precipitation SHAP values (-1.00 to 2.00) suggests threshold-  
472 dependent effects, where low precipitation events contribute negatively to drought mitigation while  
473 high precipitation provides substantial positive contributions. Temperature exhibits a more complex  
474 influence pattern, with SHAP values distributed across both positive and negative domains,  
475 reflecting its dual role in drought dynamics: moderate temperatures may enhance vegetation water  
476 use efficiency (positive contribution), while extreme temperatures intensify evapotranspiration  
477 demands and soil moisture depletion (negative contribution). Fig. 9b quantifies that precipitation  
478 and mean temperature collectively account for approximately 49.00% of the total model decision-  
479 making process, with average SHAP magnitudes of 0.282 and 0.138 respectively. Surface pressure,  
480 cloud cover, and maximum temperature demonstrate moderate but consistent influences (SHAP  
481 magnitudes of 0.053 to 0.124), likely operating through indirect pathways affecting atmospheric  
482 moisture transport, radiation balance, and boundary layer dynamics. The concentrated distribution  
483 of these secondary variables' SHAP values suggests more linear, predictable relationships with  
484 drought outcomes, contrasting with the high variability observed in precipitation and temperature  
485 effects, which reflects the non-stationary nature of hydro-climatic processes and the model's  
486 capacity to capture complex feature interactions across different drought severity conditions.



487

488

(a)



489

490

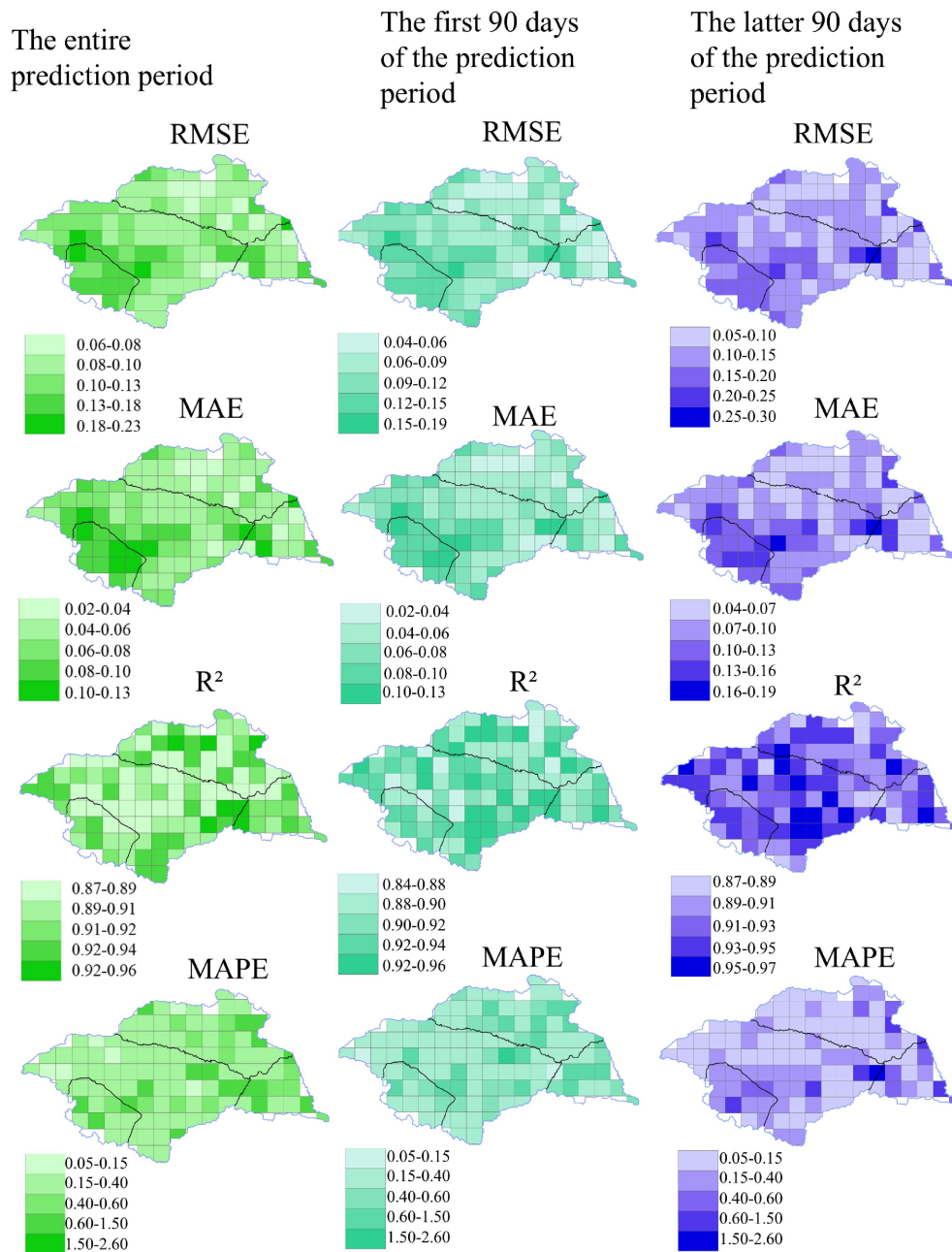
(b)

491 Figure 9 Relative contributions of meteorological variables to drought forecasting at a 180-day  
492 lead time

493 While this study demonstrates the superior performance of the VMD-informer-LSTM model  
494 through comprehensive comparative analysis, several aspects of model uncertainty warrant  
495 acknowledgement. The concentrated performance distributions observed in violin plots suggest  
496 relatively low model uncertainty across different geographical locations, with the VMD-informer-  
497 LSTM model showing the most stable performance (IQR: 0.05 for RMSE). However, systematic  
498 uncertainty quantification through techniques such as ensemble modeling, Monte Carlo dropout, or  
499 Bayesian approaches was not implemented in this study, representing a limitation that could be  
500 addressed in future research to provide confidence intervals for predictions and better understand  
501 prediction reliability under different hydroclimatic conditions.

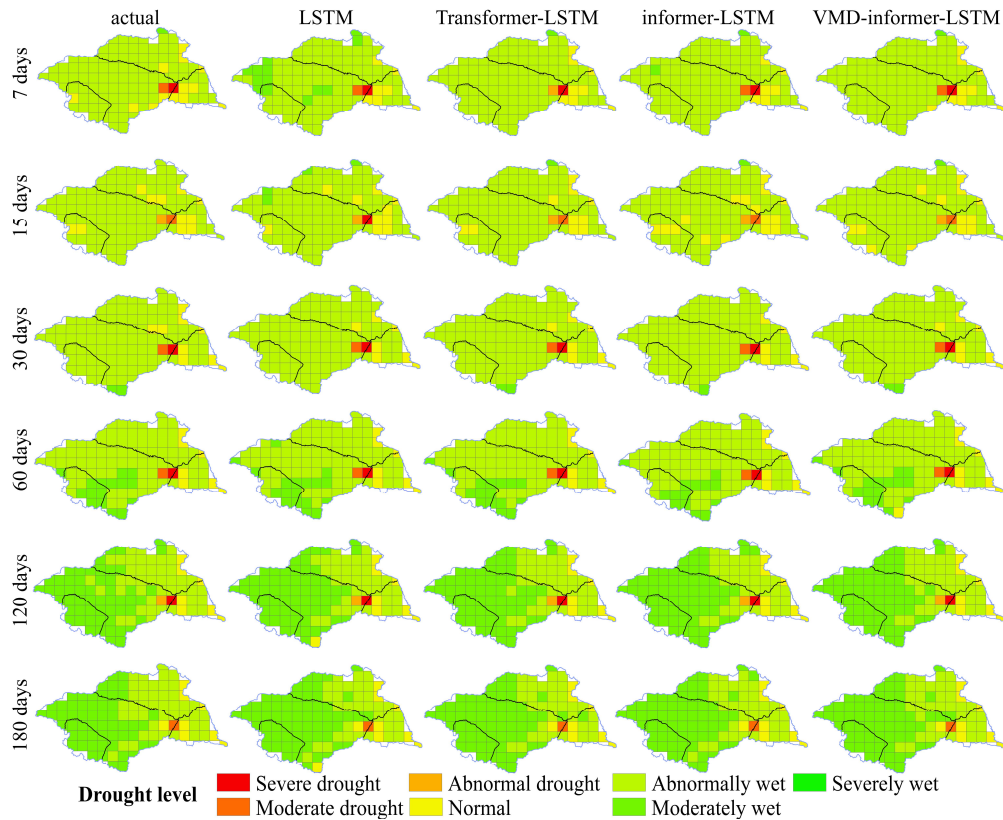
502 The spatial analysis reveals that prediction accuracy varies across the basin, with slightly  
503 higher uncertainties observed along catchment peripheries. This is potentially related to boundary  
504 effects or data quality variations. Future work should incorporate explicit uncertainty quantification  
505 methods to enhance the model's operational applicability and provide decision-makers with  
506 confidence measures alongside drought predictions.

507 Fig. 10 illustrates the spatial prediction performance of the VMD-informer-LSTM model in  
508 the Huaihe River Basin. Overall, the model achieves the highest accuracy in the first 90 days of  
509 prediction, with an  $R^2$  close to 0.92 and low error, effectively characterizing the evolution of drought.  
510 As the prediction horizon extends beyond 90 days, the accuracy shows a noticeable decline,  
511 reflecting the increasing difficulty of capturing long-term drought dynamics. In terms of spatial  
512 distribution, the upstream area performs the best, accurately reproducing the observed drought  
513 process. The downstream area follows, with the overall drought trend being tracked, though there  
514 is a tendency of underestimation in drought intensity. The midstream area shows slightly larger  
515 errors, but maintains high consistency with ERA5 reanalysis data on a long-term scale. The Yi Shu  
516 Si River region shows a relatively balanced performance, with the model effectively reflecting  
517 changes in drought levels.



518  
519

Figure 10 The spatial distribution of VMD-informer-LSTM Model performance



520

521

Figure 11 Comparison of drought forecasting model performance at different time scales

522

Fig. 11 further reveals the characteristics of drought category distribution under different prediction horizons and reflects regional differences. In the short-term predictions (first 15 days), although some models exhibit prediction errors, the overall results in the upstream, midstream, downstream, and Yi Shu Si River regions remain broadly consistent with observations. At the 7-day horizon, the LSTM misclassifies 11 grid cells, identifying the abnormally wet category as moderately wet. At 15 days, the informer-LSTM shows errors in 4 grid cells, misclassifying abnormally wet conditions as normal.

529

In the medium-term predictions (30–60 days), the VMD-informer-LSTM demonstrates the best performance, with only 2 misclassified grid cells at both horizons, whereas the other three models show larger deviations, mainly concentrated in the upstream, midstream, and Yi Shu Si River regions. In the long-term predictions (120–180 days), prediction errors increase across all models; however, the VMD-informer-LSTM continues to maintain the highest overall accuracy. Across all prediction periods, models exhibit a common tendency to underestimate drought categories, with the VMD-informer-LSTM showing the smallest degree of underestimation.

536

Overall, it can be seen that the upstream and downstream regions achieved the highest observations consistency, followed by the Yi Shu Si River region, while the midstream region performed the weakest.

538

## 539 5. Discussion

540

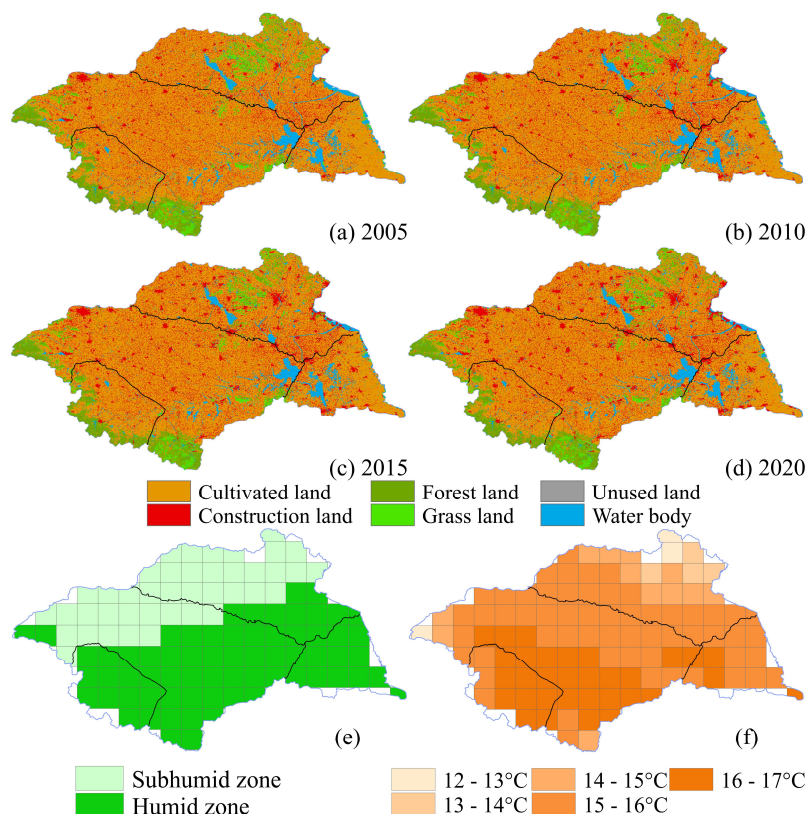
Further combining Table 2 and Fig. 12 provides a clearer understanding of the reasons for the differences in model prediction accuracy across different regions. From 2005 to 2020, the cultivated land in the basin continuously decreased (from 187,254 km<sup>2</sup> to 180,161 km<sup>2</sup>), the construction land significantly increased (from 34,739 km<sup>2</sup> to 42,801 km<sup>2</sup>), the grassland area markedly declined, and

543

544 the water area slightly increased. In the midstream region, the reduction of cultivated land, forest  
 545 land, and grassland, coupled with the increase in construction land leading to the expansion of  
 546 impervious surfaces, has altered the water cycle process. This has caused the model's prediction to  
 547 underestimate drought severity, demonstrating that environmental changes have exacerbated  
 548 hydrological droughts.

549 Table 2 Area of land use types in Huaihe River basin from 2005 to 2020(km<sup>2</sup>)

| Year | Cultivated Land | Forest land | Grassland | Water Body | Building | Unused Land |
|------|-----------------|-------------|-----------|------------|----------|-------------|
| 2005 | 187254          | 16550       | 10149     | 13159      | 34739    | 213         |
| 2010 | 186078          | 16593       | 10117     | 13224      | 35841    | 212         |
| 2015 | 184597          | 16539       | 10049     | 13326      | 37326    | 231         |
| 2020 | 180161          | 16052       | 8083      | 14282      | 42801    | 168         |



550

551 Figure 12 Distribution of Land Use, Climate Zones, and Multi-year Average Temperature in  
 552 the Huaihe River Basin (a)–(d) Spatiotemporal distribution of land use in the Huaihe River Basin  
 553 from 2005 to 2020; (e) Distribution map of semi-humid and humid zones in the Huaihe River  
 554 Basin; (f) Distribution map of multi-year average temperature in the Huaihe River Basin

555 Meanwhile, Figure 12 shows distinct climatic zone characteristics: the upstream, southern  
 556 midstream, downstream, and southern regions of the Yi Shu Si River are in the humid zone, where  
 557 the annual mean temperature in the upstream and its adjacent southern midstream regions is close  
 558 to 17°C, and the annual mean temperature in the downstream and its adjacent southern midstream  
 559 regions as well as the southern regions of the Yi Shu Si River is between 13–16°C. In contrast, the  
 560 northern midstream and northern regions of the Yi Shu Si River are in the semi-humid zone, with  
 561 an annual mean temperature between 12°C and 15°C. Overall, the prediction results of several  
 562 models underestimated hydrological drought, with misclassifications mainly concentrated in the  
 563 transition zones between the humid and semi-humid regions. The semi-humid regions showed

564 relatively more frequent errors compared to the humid regions.

565 The results show that the VMD-Informer-LSTM model exhibits high prediction accuracy  
566 within the 30–90 day forecast period at the time scale, while the prediction accuracy decreases  
567 during the longer forecast period of 120–180 days. Spatially, the prediction results for the upstream  
568 and downstream regions show the highest consistency with the ERA5 reanalysis values, followed  
569 by the Yishuisi River region, with the midstream region showing relatively weaker performance. In  
570 summary, the VMD-Informer-LSTM framework proposed in this study demonstrates significant  
571 advantages in handling drought index series with prominent non-stationarity and multi-time scale  
572 features, using a multi-scale modeling strategy of "decomposition—parallel modeling—feature  
573 fusion." On the one hand, VMD effectively reduces the complexity of the original series, allowing  
574 for the separation of variation features at different time scales and modeling them individually. On  
575 the other hand, the parallel structure of Informer and LSTM focuses on capturing long-term  
576 background state changes and short-term fluctuations, enabling the model to represent both the  
577 persistence and phase-specific fluctuations of the drought process.

578 The Huaihe River Basin is an agriculturally intensive region, where irrigation can substantially  
579 modify actual evapotranspiration and soil moisture conditions, especially during the crop growing  
580 season. Irrigation increases the water availability in croplands, enhances actual evapotranspiration,  
581 and may alleviate soil moisture deficits during dry periods. Therefore, drought prediction results in  
582 irrigated cropland areas should be interpreted with caution. Future work should incorporate spatially  
583 explicit irrigation water-use data, crop-specific water demand, ground-based soil moisture and  
584 streamflow observations, and satellite-based products such as SMAP and GRACE to further  
585 quantify and correct irrigation-related biases.

586 Moreover, the model is constructed using one-dimensional time series at individual grid points  
587 as input, without explicitly capturing the spatial propagation of drought, thereby neglecting the  
588 spatial interconnections among different regions. Future work will incorporate multi-source  
589 observational data and develop spatio-temporal coupling modelling approaches to enhance the  
590 representation of drought evolution processes, thereby improving the reliability of predictions.

## 591 6. Conclusion

592 This study takes the Huaihe River Basin in China as an example and constructs the VMD-  
593 informer-LSTM model, and compares it with the LSTM, Transformer-LSTM, and informer-LSTM  
594 models to verify its ability to predict hydrological drought in both temporal and spatial dimensions,  
595 and influencing factors are quantitatively analyzed. The main conclusions are as follows:

596 (1) The VMD-informer-LSTM model shows clear advantages in drought forecasting across  
597 different lead times and drought severity levels. Compared with the baseline LSTM, it improves  $R^2$   
598 by 28.4% ( $0.7156 \rightarrow 0.9191$ ) and reduces RMSE by 46.2% ( $0.2087 \rightarrow 0.1122$ ). Further  
599 comparisons reveal that the single LSTM struggles to capture the complex drought process and  
600 performs the poorest in all models' predictions. Transformer-LSTM improves accuracy to some  
601 extent, but there is still significant error accumulation in long-term predictions. The informer-LSTM,  
602 leveraging the sparse self-attention mechanism and generative decoding approach of the informer,  
603 can balance efficiency and accuracy in long time series prediction, showing greater stability than  
604 Transformer-LSTM and being the best among the three benchmark models. However, the VMD-  
605 informer-LSTM, by introducing VMD decomposition to further extract multi-scale features and  
606 combining the long sequence modeling advantages of the informer with the local dynamic

607 characterization ability of LSTM, achieves multi-level information fusion. Therefore, the VMD-  
608 informer-LSTM model achieves the highest precision in short-term forecasting (7 days), has the  
609 smallest error growth rate in the medium term (30–60 days), and can still more effectively  
610 characterize the evolution of drought in the long term (120–180 days). Its underestimation of  
611 drought intensity is significantly lower than other models.

612 (2) The spatial prediction performance of the VMD informant LSTM model is influenced by  
613 land use and climate regions. Within the entire watershed, all models showed excellent prediction  
614 performance within a 30 day prediction period, with the VMD-informer-LSTM model being the  
615 most accurate. However, within a prediction period of 120-180 days, the prediction accuracy of all  
616 models significantly decreased throughout the watershed. Overall, the predicted drought intensity  
617 was relatively mild, with misclassifications mainly concentrated in the transition zones between the  
618 humid and semi-humid regions, and errors occurring more frequently in the semi-humid regions  
619 compared to the humid regions. The model performs best in the upstream region, followed by the  
620 downstream and Yishus River regions, while prediction accuracy in the midstream region is  
621 relatively weak. With the extension of the forecast lead time, this downward trend is most evident  
622 in the middle reaches, where the reduction of arable land, grassland, and forest land, as well as the  
623 expansion of construction land, have changed the water cycle process, indicating that human  
624 activities have exacerbated drought.

625 (3) The SHAP analysis enhances the interpretability of the VMD-informer-LSTM model by  
626 revealing the relative importance of meteorological variables in drought prediction. Precipitation is  
627 the dominant factor, contributing about 28.2% to model decisions, followed by mean temperature  
628 (13.8%), while surface pressure, cloud cover, and maximum temperature together account for about  
629 15–20%. These results confirm that the model effectively identifies key meteorological drivers and  
630 enhances the interpretability of drought forecasting.

## 631 Author Contributions:

632 Conceptualization: Min Li, Ming Ou, Yuhang Yao, Changman Yin

633 Data curation: Ming Ou

634 Formal analysis: Min Li, Ming Ou

635 Funding acquisition: Min Li

636 Investigation: Min Li, Ming Ou

637 Methodology: Min Li, Ming Ou

638 Software: Min Li

639 Supervision: Ming Ou, Yuhang Yao, Changman Yin

640 Validation: Min Li

641 Visualization: Ming Ou, Yuhang Yao, Changman Yin

642 Writing – original draft: Min Li, Ming Ou

643 Writing – review & editing: Yuhang Yao, Changman Yin

## 644 Declaration of competing interest

645 The authors declare no conflicts of interest relevant to this study.

## 646 Data Availability Statement

647 The gridded daily precipitation, evaporation, potential evaporation, mean temperature,

648 maximum temperature, cloud cover, surface pressure, and wind speed data with a spatial r  
649 esolution of 0.25° were obtained from ERA5 post-processed daily statistics on single level  
650 s from 1940 to present (<https://cds.climate.copernicus.eu/datasets/derived-era5-single-levels-daily-statistics?tab=overview>), covering the period from January 1, 1984, to December 31, 20  
651 24. Concurrently, the land use data were sourced from the Chinese Academy of Sciences  
652 Resource and Environment Science Data Center (<https://www.resdc.cn/Default.aspx>). The co  
653 re implementation of the VMD–Informer–LSTM model used in this study is publicly avail  
654 able on GitHub at: <https://github.com/OUman648/vmd-informer-LSTM>.

## 656 Acknowledgements

657 This work was funded by Basic Research Program of Jiangsu, BK20250906 and Open Research  
658 Fund Program of National Key Laboratory of Water Disaster Prevention, 2024490711.

## 659 References

- 660 AghaKouchak, A., Farahmand, A., Melton, F. S., Teixeira, J., Anderson, M. C., Wardlow, B. D., &  
661 Hain, C. R. (2015). Remote sensing of drought: Progress, challenges and opportunities.  
662 *Reviews of Geophysics*, 53(2), 452–480. <https://doi.org/10.1002/2014RG000456>
- 663 Alsubih, M., Mallick, J., Talukdar, S., Salam, R., AlQadhi, S., Fattah, Md. A., & Thanh, N. V. (2021).  
664 An investigation of the short-term meteorological drought variability over Asir Region of Saudi  
665 Arabia. *Theoretical and Applied Climatology*, 145(1–2), 597–617.  
666 <https://doi.org/10.1007/s00704-021-03647-4>
- 667 Belayneh, A., Adamowski, J., Khalil, B., & Ozga-Zielinski, B. (2014). Long-term SPI drought  
668 forecasting in the Awash River Basin in Ethiopia using wavelet neural network and wavelet  
669 support vector regression models. *Journal of Hydrology*, 508, 418–429.  
670 <https://doi.org/10.1016/j.jhydrol.2013.10.052>
- 671 Bengio, Y., Courville, A., & Vincent, P. (2013). Representation Learning: A Review and New  
672 Perspectives. *IEEE Transactions on Pattern Analysis and Machine Intelligence*, 35(8), 1798–  
673 1828. <https://doi.org/10.1109/TPAMI.2013.50>
- 674 Box, G. E., Jenkins, G. M., Reinsel, G. C., & Ljung, G. M. (2015). *Time series analysis: Forecasting  
675 and control*. John Wiley & Sons.
- 676 Cook, B. I., Mankin, J. S., Marvel, K., Williams, A. P., Smerdon, J. E., & Anchukaitis, K. J. (2020).  
677 Twenty-First Century Drought Projections in the CMIP6 Forcing Scenarios. *Earth's Future*,  
678 8(6), e2019EF001461. <https://doi.org/10.1029/2019EF001461>
- 679 Dai, A. (2013). Increasing drought under global warming in observations and models. *Nature  
680 Climate Change*, 3(1), 52–58. <https://doi.org/10.1038/nclimate1633>
- 681 Dragomiretskiy, K., & Zosso, D. (2014). Variational Mode Decomposition. *IEEE Transactions on  
682 Signal Processing*, 62(3), 531–544. <https://doi.org/10.1109/TSP.2013.2288675>
- 683 Dutra, E., Wetterhall, F., Di Giuseppe, F., Naumann, G., Barbosa, P., Vogt, J., Pozzi, W., &  
684 Pappenberger, F. (2014). Global meteorological drought – Part 1: Probabilistic monitoring.  
685 *Hydrology and Earth System Sciences*, 18(7), 2657–2667. [https://doi.org/10.5194/hess-18-  
686 2657-2014](https://doi.org/10.5194/hess-18-2657-2014)
- 687 Ek, M. B., Mitchell, K. E., Lin, Y., Rogers, E., Grunmann, P., Koren, V., Gayno, G., & Tarpley, J.  
688 D. (2003). Implementation of Noah land surface model advances in the National Centers for  
689 Environmental Prediction operational mesoscale Eta model. *Journal of Geophysical Research*:

690 *Atmospheres*, 108(D22), 2002JD003296. <https://doi.org/10.1029/2002JD003296>

691 Gao, C., Zhang, Z., Zhai, J., Qing, L., & Mengting, Y. (2015). Research on meteorological  
692 thresholds of drought and flood disaster: A case study in the Huai River Basin, China.  
693 *Stochastic Environmental Research and Risk Assessment*, 29(1), 157–167.  
694 <https://doi.org/10.1007/s00477-014-0951-y>

695 Greff, K., Srivastava, R. K., Koutník, J., Steunebrink, B. R., & Schmidhuber, J. (2017). LSTM: A  
696 Search Space Odyssey. *IEEE Transactions on Neural Networks and Learning Systems*, 28(10),  
697 2222–2232. <https://doi.org/10.1109/TNNLS.2016.2582924>

698 Hao, Z., Hao, F., Singh, V. P., Ouyang, W., & Cheng, H. (2017). An integrated package for drought  
699 monitoring, prediction and analysis to aid drought modeling and assessment. *Environmental*  
700 *Modelling & Software*, 91, 199–209. <https://doi.org/10.1016/j.envsoft.2017.02.008>

701 Hersbach, H., Bell, B., Berrisford, P., Hirahara, S., Horányi, A., Muñoz-Sabater, J., Nicolas, J.,  
702 Peubey, C., Radu, R., Schepers, D., Simmons, A., Soci, C., Abdalla, S., Abellan, X., Balsamo,  
703 G., Bechtold, P., Biavati, G., Bidlot, J., Bonavita, M., ... Thépaut, J. (2020). The ERA5 global  
704 reanalysis. *Quarterly Journal of the Royal Meteorological Society*, 146(730), 1999–2049.  
705 <https://doi.org/10.1002/qj.3803>

706 Hochreiter, S., & Schmidhuber, J. (1997). Long Short-Term Memory. *Neural Computation*, 9(8),  
707 1735–1780. <https://doi.org/10.1162/neco.1997.9.8.1735>

708 Huang, S., Huang, Q., Chang, J., Zhu, Y., Leng, G., & Xing, L. (2015). Drought structure based on  
709 a nonparametric multivariate standardized drought index across the Yellow River basin, China.  
710 *Journal of Hydrology*, 530, 127–136. <https://doi.org/10.1016/j.jhydrol.2015.09.042>

711 Jacob, D., Petersen, J., Eggert, B., Alias, A., Christensen, O. B., Bouwer, L. M., Braun, A., Colette,  
712 A., Déqué, M., Georgievski, G., Georgopoulou, E., Gobiet, A., Menut, L., Nikulin, G., Haensler,  
713 A., Hempelmann, N., Jones, C., Keuler, K., Kovats, S., ... Yiou, P. (2014). EURO-CORDEX:  
714 New high-resolution climate change projections for European impact research. *Regional*  
715 *Environmental Change*, 14(2), 563–578. <https://doi.org/10.1007/s10113-013-0499-2>

716 Jaseena, K. U., & Koor, B. C. (2022). Deterministic weather forecasting models based on  
717 intelligent predictors: A survey. *Journal of King Saud University - Computer and Information*  
718 *Sciences*, 34(6, Part B), 3393–3412. <https://doi.org/10.1016/j.jksuci.2020.09.009>

719 Johny, K., Pai, M. L., & S., A. (2022). A multivariate EMD-LSTM model aided with Time  
720 Dependent Intrinsic Cross-Correlation for monthly rainfall prediction. *Applied Soft Computing*,  
721 123, 108941. <https://doi.org/10.1016/j.asoc.2022.108941>

722 Kratzert, F., Klotz, D., Brenner, C., Schulz, K., & Herrnegger, M. (2018). Rainfall–runoff modelling  
723 using Long Short-Term Memory (LSTM) networks. *Hydrology and Earth System Sciences*,  
724 22(11), 6005–6022. <https://doi.org/10.5194/hess-22-6005-2018>

725 Lawrence, D. M., Oleson, K. W., Flanner, M. G., Thornton, P. E., Swenson, S. C., Lawrence, P. J.,  
726 Zeng, X., Yang, Z.-L., Levis, S., Sakaguchi, K., Bonan, G. B., & Slater, A. G. (2011).  
727 Parameterization improvements and functional and structural advances in Version 4 of the  
728 Community Land Model: PARAMETERIZATION IMPROVEMENTS AND FUNCTIONAL  
729 AND STRUCTURAL ADVANCES. *Journal of Advances in Modeling Earth Systems*, 3(1),  
730 n/a-n/a. <https://doi.org/10.1029/2011MS00045>

731 LeCun, Y., Bengio, Y., & Hinton, G. (2015). Deep learning. *Nature*, 521(7553), 436–444.  
732 <https://doi.org/10.1038/nature14539>

733 Li, Z., Wu, H., Duan, S., Zhao, W., Ren, H., Liu, X., Leng, P., Tang, R., Ye, X., Zhu, J., Sun, Y., Si,

734 M., Liu, M., Li, J., Zhang, X., Shang, G., Tang, B., Yan, G., & Zhou, C. (2023). Satellite  
735 Remote Sensing of Global Land Surface Temperature: Definition, Methods, Products, and  
736 Applications. *Reviews of Geophysics*, *61*(1), e2022RG000777.  
737 <https://doi.org/10.1029/2022RG000777>

738 Lundberg, S., & Lee, S.-I. (2017). *A Unified Approach to Interpreting Model Predictions*  
739 (arXiv:1705.07874; Version 2). arXiv. <https://doi.org/10.48550/arXiv.1705.07874>

740 Mishra, A. K., & Desai, V. R. (2005). Drought forecasting using stochastic models. *Stochastic*  
741 *Environmental Research and Risk Assessment*, *19*(5), 326–339.  
742 <https://doi.org/10.1007/s00477-005-0238-4>

743 Mo, K. C. (2008). Model-Based Drought Indices over the United States. *Journal of*  
744 *Hydrometeorology*, *9*(6), 1212–1230. <https://doi.org/10.1175/2008JHM1002.1>

745 Modarres, R. (2007). Streamflow drought time series forecasting. *Stochastic Environmental*  
746 *Research and Risk Assessment*, *21*(3), 223–233. <https://doi.org/10.1007/s00477-006-0058-1>

747 Morid, S., Smakhtin, V., & Moghaddasi, M. (2006). Comparison of seven meteorological indices  
748 for drought monitoring in Iran. *International Journal of Climatology*, *26*(7), 971–985.  
749 <https://doi.org/10.1002/joc.1264>

750 Mosavi, A., Ozturk, P., & Chau, K. (2018). Flood Prediction Using Machine Learning Models:  
751 Literature Review. *Water*, *10*(11), 1536. <https://doi.org/10.3390/w10111536>

752 Mossad, A., & Alazba, A. (2015). Drought Forecasting Using Stochastic Models in a Hyper-Arid  
753 Climate. *Atmosphere*, *6*(4), 410–430. <https://doi.org/10.3390/atmos6040410>

754 Muñoz-Sabater, J., Dutra, E., Agustí-Panareda, A., Albergel, C., Arduini, G., Balsamo, G., Boussetta,  
755 S., Choulga, M., Harrigan, S., Hersbach, H., Martens, B., Miralles, D. G., Piles, M., Rodríguez-  
756 Fernández, N. J., Zsoter, E., Buontempo, C., & Thépaut, J.-N. (2021). ERA5-Land: A state-of-  
757 the-art global reanalysis dataset for land applications. *Earth System Science Data*, *13*(9), 4349–  
758 4383. <https://doi.org/10.5194/essd-13-4349-2021>

759 Myttenaere, A. D., Golden, B., Grand, B. L., & Rossi, F. (2016). Mean Absolute Percentage Error  
760 for regression models. *Neurocomputing*, *192*, 38–48.  
761 <https://doi.org/10.1016/j.neucom.2015.12.114>

762 Nash, J. E., & Sutcliffe, J. V. (1970). River flow forecasting through conceptual models part I—A  
763 discussion of principles. *Journal of Hydrology*, *10*(3), 282–290.

764 Pozzi, W., Sheffield, J., Stefanski, R., Cripe, D., Pulwarty, R., Vogt, J. V., Heim, R. R., Brewer, M.  
765 J., Svoboda, M., Westerhoff, R., Van Dijk, A. I. J. M., Lloyd-Hughes, B., Pappenberger, F.,  
766 Werner, M., Dutra, E., Wetterhall, F., Wagner, W., Schubert, S., Mo, K., ... Lawford, R. (2013).  
767 Toward Global Drought Early Warning Capability: Expanding International Cooperation for  
768 the Development of a Framework for Monitoring and Forecasting. *Bulletin of the American*  
769 *Meteorological Society*, *94*(6), 776–785. <https://doi.org/10.1175/BAMS-D-11-00176.1>

770 Rummukainen, M. (2010). State-of-the-art with regional climate models. *WIREs Climate Change*,  
771 *1*(1), 82–96. <https://doi.org/10.1002/wcc.8>

772 Saha, S., Moorthi, S., Wu, X., Wang, J., Nadiga, S., Tripp, P., Behringer, D., Hou, Y.-T., Chuang, H.,  
773 Iredell, M., Ek, M., Meng, J., Yang, R., Mendez, M. P., Van Den Dool, H., Zhang, Q., Wang,  
774 W., Chen, M., & Becker, E. (2014). The NCEP Climate Forecast System Version 2. *Journal of*  
775 *Climate*, *27*(6), 2185–2208. <https://doi.org/10.1175/JCLI-D-12-00823.1>

776 Schmidhuber, J. (2015). Deep learning in neural networks: An overview. *Neural Networks*, *61*, 85–  
777 117. <https://doi.org/10.1016/j.neunet.2014.09.003>

778 Shlezinger, N., Whang, J., Eldar, Y. C., & Dimakis, A. G. (2023). Model-Based Deep Learning.  
779 *Proceedings of the IEEE*, *111*(5), 465–499. <https://doi.org/10.1109/JPROC.2023.3247480>

780 Sit, M., Demiray, B. Z., Xiang, Z., Ewing, G. J., Sermet, Y., & Demir, I. (2020). A comprehensive  
781 review of deep learning applications in hydrology and water resources. *Water Science and*  
782 *Technology*, *82*(12), 2635–2670. <https://doi.org/10.2166/wst.2020.369>

783 Svoboda, M., LeCompte, D., Hayes, M., Heim, R., Gleason, K., Angel, J., Rippey, B., Tinker, R.,  
784 Palecki, M., Stooksbury, D., Miskus, D., & Stephens, S. (2002). THE DROUGHT MONITOR.  
785 *Bulletin of the American Meteorological Society*, *83*(8), 1181–1190.  
786 <https://doi.org/10.1175/1520-0477-83.8.1181>

787 Trenberth, K. E., Dai, A., Van Der Schrier, G., Jones, P. D., Barichivich, J., Briffa, K. R., & Sheffield,  
788 J. (2014). Global warming and changes in drought. *Nature Climate Change*, *4*(1), 17–22.  
789 <https://doi.org/10.1038/nclimate2067>

790 Vaswani, A., Shazeer, N., Parmar, N., Uszkoreit, J., Jones, L., Gomez, A. N., Kaiser, L., &  
791 Polosukhin, I. (2017). Attention is all you need. *Advances in Neural Information Processing*  
792 *Systems*, *30*(1), 5998–6008.

793 Vicente-Serrano, S. M., Miralles, D. G., Domínguez-Castro, F., Azorin-Molina, C., El Kenawy, A.,  
794 McVicar, T. R., Tomás-Burguera, M., Beguería, S., Maneta, M., & Peña-Gallardo, M. (2018).  
795 Global Assessment of the Standardized Evapotranspiration Deficit Index (SEDI) for Drought  
796 Analysis and Monitoring. *Journal of Climate*, *31*(14), 5371–5393.  
797 <https://doi.org/10.1175/JCLI-D-17-0775.1>

798 Wang, H., Liang, Q., Hancock, J. T., & Khoshgoftaar, T. M. (2024). Feature selection strategies: A  
799 comparative analysis of SHAP-value and importance-based methods. *Journal of Big Data*,  
800 *11*(1), 44. <https://doi.org/10.1186/s40537-024-00905-w>

801 Willmott, C., & Matsuura, K. (2005). Advantages of the mean absolute error (MAE) over the root  
802 mean square error (RMSE) in assessing average model performance. *Climate Research*, *30*,  
803 79–82. <https://doi.org/10.3354/cr030079>

804 Wood, A. W., Hopson, T., Newman, A., Brekke, L., Arnold, J., & Clark, M. (2016). Quantifying  
805 Streamflow Forecast Skill Elasticity to Initial Condition and Climate Prediction Skill. *Journal*  
806 *of Hydrometeorology*, *17*(2), 651–668. <https://doi.org/10.1175/JHM-D-14-0213.1>

807 Yao, T., Zhao, Q., Wu, C., Hu, X., Xia, C., Wang, X., Sang, G., Liu, J., & Wang, H. (2024). Spatio-  
808 temporal Variation Characteristics of Extreme Climate Events and Their Teleconnections to  
809 Large-scale Ocean-atmospheric Circulation Patterns in Huaihe River Basin, China During  
810 1959–2019. *Chinese Geographical Science*, *34*(1), 118–134. <https://doi.org/10.1007/s11769-023-1398-1>

812 Yuan, S., & Quiring, S. M. (2017). Evaluation of soil moisture in CMIP5 simulations over the  
813 contiguous United States using in situ and satellite observations. *Hydrology and Earth System*  
814 *Sciences*, *21*(4), 2203–2218. <https://doi.org/10.5194/hess-21-2203-2017>

815 Zhang, J., Xin, X., Shang, Y., Wang, Y., & Zhang, L. (2023). Nonstationary significant wave height  
816 forecasting with a hybrid VMD-CNN model. *Ocean Engineering*, *285*, 115338.  
817 <https://doi.org/10.1016/j.oceaneng.2023.115338>

818 Zhang, L., Lin, J., Liu, B., Zhang, Z., Yan, X., & Wei, M. (2019). A Review on Deep Learning  
819 Applications in Prognostics and Health Management. *IEEE Access*, *7*, 162415–162438.  
820 <https://doi.org/10.1109/ACCESS.2019.2950985>

821 Zhang, Q., Kong, D., Shi, P., Singh, V. P., & Sun, P. (2018). Vegetation phenology on the Qinghai-

822 Tibetan Plateau and its response to climate change (1982–2013). *Agricultural and Forest*  
823 *Meteorology*, 248, 408–417. <https://doi.org/10.1016/j.agrformet.2017.10.026>

824 Zhang, Q., Zhang, J., Yan, D., & Wang, Y. (2014). Extreme precipitation events identified using  
825 detrended fluctuation analysis (DFA) in Anhui, China. *Theoretical and Applied Climatology*,  
826 117(1–2), 169–174. <https://doi.org/10.1007/s00704-013-0986-x>

827 Zhang, X., Duan, Y., Duan, J., Jian, D., & Ma, Z. (2022). A daily drought index based on  
828 evapotranspiration and its application in regional drought analyses. *Science China Earth*  
829 *Sciences*, 65(2), 317–336. <https://doi.org/10.1007/s11430-021-9822-y>

830 Zhao, L., Li, Z., Qu, L., Zhang, J., & Teng, B. (2023). A hybrid VMD-LSTM/GRU model to predict  
831 non-stationary and irregular waves on the east coast of China. *Ocean Engineering*, 276, 114136.  
832 <https://doi.org/10.1016/j.oceaneng.2023.114136>

833 Zhou, H., Zhang, S., Peng, J., Zhang, S., Li, J., Xiong, H., & Zhang, W. (2021a). Informer: Beyond  
834 Efficient Transformer for Long Sequence Time-Series Forecasting. *Proceedings of the AAAI*  
835 *Conference on Artificial Intelligence*, 35(12), 11106–11115.  
836 <https://doi.org/10.1609/aaai.v35i12.17325>

837 Zhou, H., Zhang, S., Peng, J., Zhang, S., Li, J., Xiong, H., & Zhang, W. (2021b). Informer: Beyond  
838 Efficient Transformer for Long Sequence Time-Series Forecasting. *Proceedings of the AAAI*  
839 *Conference on Artificial Intelligence*, 35(12), 11106–11115.  
840 <https://doi.org/10.1609/aaai.v35i12.17325>

841 Zuo, G., Luo, J., Wang, N., Lian, Y., & He, X. (2020). Decomposition ensemble model based on  
842 variational mode decomposition and long short-term memory for streamflow forecasting.  
843 *Journal of Hydrology*, 585, 124776. <https://doi.org/10.1016/j.jhydrol.2020.124776>

844